



Variability of the Pacific-derived Arctic water over the southeastern Wandel Sea shelf (Northeast Greenland) in 2015-2016

Dmitrenko, Igor A.; Kirillov, Sergei A.; Rudels, Bert; Babb, David G.; Myers, Paul G. ; Stedmon, Colin A.; Bendtsen, Jørgen ; Ehn, Jens K.; Pedersen, Leif Toudal; Rysgaard, Søren

Total number of authors:
11

Published in:
Journal of Geophysical Research: Atmospheres

Link to article, DOI:
[10.1029/2018JC014567](https://doi.org/10.1029/2018JC014567)

Publication date:
2019

Document Version
Peer reviewed version

[Link back to DTU Orbit](#)

Citation (APA):
Dmitrenko, I. A., Kirillov, S. A., Rudels, B., Babb, D. G., Myers, P. G., Stedmon, C. A., Bendtsen, J., Ehn, J. K., Pedersen, L. T., Rysgaard, S., & Barber, D. G. (2019). Variability of the Pacific-derived Arctic water over the southeastern Wandel Sea shelf (Northeast Greenland) in 2015-2016. *Journal of Geophysical Research: Atmospheres*, 124(1), 349-373. <https://doi.org/10.1029/2018JC014567>

General rights

Copyright and moral rights for the publications made accessible in the public portal are retained by the authors and/or other copyright owners and it is a condition of accessing publications that users recognise and abide by the legal requirements associated with these rights.

- Users may download and print one copy of any publication from the public portal for the purpose of private study or research.
- You may not further distribute the material or use it for any profit-making activity or commercial gain
- You may freely distribute the URL identifying the publication in the public portal

If you believe that this document breaches copyright please contact us providing details, and we will remove access to the work immediately and investigate your claim.

20 **Abstract:** A portion of the freshwater transport through Fram Strait consists of low salinity
21 Pacific-derived Arctic water flowing southward along the east coast of Greenland. The pathways
22 of this water are currently unclear. An Ice Tethered Profiler deployed over the southeastern
23 Wandel Sea shelf (Northeast Greenland) in May 2015 collected a profile every 3 hours for a year
24 recording salinity-temperature-depth (CTD) and Colored Dissolved Organic Matter (CDOM)
25 fluorescence. This was accompanied by velocity observations. The CTD data revealed that the
26 sub-surface water (~15-85 m depth) characterised by high CDOM resembles the “cold Halostad”
27 in the Canada Basin formed by the injection of Pacific water. We suggest that the coastal branch
28 of the Pacific water outflow from the Arctic Ocean supplies the Wandel Sea halostad. The
29 halostad has a clear seasonal pattern. From July to October-November, it is shallow, more saline,
30 warmer, and with less CDOM. From November to April, the halostad deepens, cools, freshens
31 and CDOM increases, likely indicating a higher fraction of the Pacific winter water. The CTD
32 survey, wind and current data, and numerical simulations show that the seasonal variation of
33 wind over the continental slope likely controls seasonal changes of the intermediate water layer.
34 Over northeast Greenland, winter winds have a northerly component from November to April,
35 favouring Ekman transport of the Pacific-derived water to the Wandel Sea shelf. In contrast, the
36 prevailing southerly summer winds result in retreat of the Pacific-derived water off the shelf. The
37 landfast ice off-slope extension modifies wind-forcing disrupting seasonal patterns.

38

- 39 • The Pacific-derived Arctic water modifies structure of the Wandel Sea halocline;
- 40 • During winter, northerly winds force the on-shelf Ekman transport of Pacific water (PW);
- 41 • During summer, southerly winds favour coastal upwelling forcing PW off-shelf.

42 **1. Introduction**

43 Low salinity water from the Pacific significantly contributes to the Arctic Ocean freshwater budget
44 [Serreze *et al.*, 2006], which is also changing as a result of ongoing climate change [Holland *et*
45 *al.*, 2007; Rodell *et al.*, 2018]. Pacific water (PW) enters the Arctic Ocean through Bering Strait
46 and spreads over the Arctic Ocean following two major pathways, a Transpolar branch crossing
47 the Arctic Ocean to Fram Strait and an Alaskan branch along the Beaufort Sea continental slope

48 through the Canadian Archipelago to Baffin Bay – Figure 1 [e.g., *Hu and Myers*, 2013; *Watanabe*,
49 2013; *Aksenov et al.*, 2016]. This has been confirmed by the PW tracers detected in western Fram
50 Strait, along northeast Greenland and in Baffin Bay [e.g., *Jones et al.*, 1998, 2003; *Falck* 2001;
51 *Amon et al.*, 2003; *Dodd et al.*, 2009, 2012, *Alkire et al.*, 2010]. The Pacific-derived Arctic water
52 comprises up to 20% of the freshwater inventory in the upper 300 m in western Fram Strait [*Dodd*
53 *et al.*, 2012] and dominates the freshwater inventory over the top 150 meters in western Davis
54 Strait [*Alkire et al.*, 2010].

55 Climate change in the Arctic is manifested in the increasing freshwater content over the
56 last several decades [*Prowse et al.*, 2015]. Recent increases in Arctic freshwater flux are primarily
57 attributed to precipitation, river runoff and sea-ice melt [*Rabe et al.*, 2011, *Haine et al.*, 2015].
58 Over the coastal domains of eastern Greenland and in Baffin Bay, there are additional contributions
59 from glacial melt [*Bamber et al.*, 2018; *Castro de la Guardia et al.*, 2015; *Bendtsen et al.*, 2017]
60 superimposed on Arctic freshwater flux including a variable PW fraction. Over the northwest
61 Greenland shelf and coastal domains, the glacier meltwater fraction can also be significant
62 [*Stedmon et al.*, 2015; *Bendtsen et al.*, 2017]. The PW outflow complicates the direct estimates of
63 the glacier meltwater fraction. The general contribution of the Pacific-derived Arctic water to the
64 freshwater inventory remains poorly understood, partly due to seasonal and interannual variability
65 of the PW inflow and outflow to/from the Arctic Ocean [e.g., *Woodgate et al.*, 2005, 2012; *Falck*
66 *et al.*, 2005; *Dodd et al.*, 2012; *de Steur et al.*, 2013], but also because of the different pathways of
67 PW in the Arctic Ocean [*Hu and Myers*, 2013; *Aksenov et al.*, 2016]. The coastal branch of the
68 PW outflow through western Fram Strait is poorly resolved due to insufficient data coverage [e.g.,
69 *Falck* 2001; *Dmitrenko et al.*, 2017], however, numerical simulations indicate its presence [*Hu*
70 *and Myers*, 2013, *Aksenov et al.*, 2016] and PW is clearly observed downstream along the southeast

71 coast of Greenland [e.g., *Bacon et al.*, 2002; *Jones et al.*, 2003; *Sutherland and Pickart*, 2008;
72 *Sutherland et al.* 2009].

73 In the Canada Basin, the relatively fresh PW impacts the halocline structure, producing a
74 double halocline layer with a low stratified “cold Halostad” formed by insertion of the cold winter
75 PW that overlies Lower Halocline Water originating from the Eurasian Basin [*McLaughlin et al.*,
76 2004; *Shimada et al.*, 2005]. The Arctic halocline water is also characterised by a high content of
77 colored dissolved organic matter (CDOM), which can be traced using fluorometers [*Guay et al.*,
78 1999]. CDOM in halocline waters from Eurasian and Canada Basins differ in that. While the
79 Eurasian halocline has a high content of terrestrial organic matter from Siberian rivers, the Canada
80 Basin halocline CDOM primarily originates from autochthonous production over the productive
81 Chukchi shelf region [*Stedmon et al.*, 2011]. The low-salinity surface polar water including low-
82 salinity water of Pacific origin and halocline water leaving the Arctic Ocean through Fram Strait
83 partly passes over the shelf area of the Wandel Sea. Following *Dmitrenko et al.* [2017], we use the
84 physical and chemical characteristics mentioned above to detect and trace the Pacific-derived
85 water fraction of the Arctic Ocean outflow on the Northeast Greenland shelf (Figure 2).

86 The landfast ice-tethered mooring was deployed for one year from 15 May 2015 to 6 April
87 2016 over the southeast Wandel Sea outer shelf (Figure 2b). Mooring deployment was
88 complemented by the conductivity-temperature-depth (CTD) survey occupied in April-May and
89 August 2015, and April 2016 over the southeast Wandel Sea shelf from the landfast ice during
90 spring and in open water during summer (Figures 3-5). This project was conducted under the
91 framework of the Arctic Science Partnership (ASP) as part of the first scientific expedition based
92 at the new Villum Research Station located at the Danish military outpost Station Nord. Our
93 objectives here are to explore this data set along with results of PW passive tracers from a high
94 resolution numerical simulation to assess spatial and temporal variability of the Pacific-derived

95 halostad. We hypothesise that variability is driven by lateral displacement of the PW bearing
96 coastal jet, which is suggested to flow along the shelfbreak of northeast Greenland (Figure 2b).
97 Here we focus on the halostad observed in the 15-85 m depth range, and more specifically on its
98 cooler part at 55-85 m depth, which shows most significant seasonal and spatial variability.

99 The Wandel Sea represents a glacial inlet comprised by several fjords open to the northeast
100 Greenland continental slope (Figure 2). It is covered by landfast sea ice all year around, and only
101 the interior of fjords becomes ice free during August-September (Figure 2b). Note that in August
102 2016 the multiyear landfast ice bridge over the Wandel Sea outer shelf became unstable, and a
103 sizeable portion to the east of Prinsesse Margreth Island collapsed in August 2017. The ice edge
104 to the east roughly delineates the Wandel Sea continental shelf break, which is where a coastal
105 polynya opens in response to southerly winds. The Wandel Sea shelf bottom topography is poorly
106 known. The most comprehensive bathymetry data set compiled by *Nørgaard-Pedersen et al.*
107 [2016] revealed a glacier trough in front of the northern outlet of the Flade Isblink Ice Cap, an
108 isolated ice cap with a surface area of 5 000 km² and maximum thickness of 600 m [e.g., *Palmer*
109 *et al.*, 2010; *Rinne et al.*, 2011]. The glacial trough is open to the continental slope with depth
110 varying from ~130 m at the tidewater glacier terminus to about 180 m depth at mooring location
111 (Figure 3). This allows the Atlantic-derived Arctic water to flow into the Wandel Sea shelf at
112 depths greater than 140 m [*Dmitrenko et al.*, 2017; *Limoges et al.*, 2018]. The glacier trough is
113 flanked on both sides by numerous icebergs (Figure 3b) that are grounded on the marginal lateral
114 moraine reducing lateral exchange with ambient water from the continental slope for depths
115 exceeding ~80 m (Figures 3a and 4). The glacier trough area is separated laterally from the mid-
116 shelf by ~20-30 m deep shoals preventing the halostad to extend over the entire Wandel Sea shelf
117 (Figure 3a).

118 Prior to the field programs in 2015-2016, there were no oceanographic data collected over
119 the Wandel Sea shelf. In contrast, the more easily accessible downstream Northeast Water Polynya
120 (NEW) area (Figure 2b) was well explored during the polynya-focused international programs in
121 1992-1993 [e.g., *Bignami and Hopkins, 1997; Budéus et al., 1997*]. Using this data set, *Falck*
122 [2001] was first to suggest a Pacific origin for the NEW on-shelf halostad. Following *Falck* [2001]
123 and using recent CTD observations, *Dmitrenko et al.* [2017] suggested that the coastal branch of
124 the Pacific-derived Arctic water flowing along the upper Wandel Sea continental slope was the
125 source of the cold halostad in the Wandel Sea (Figure 2b). Using a 3-week time series from the
126 landfast ice-tethered mooring deployed at the front of the northern outlet of the Flade Isblink Ice
127 Cap in April 2015 (Figure 3), *Kirillov et al.* [2017] reported on storm induced downwelling with
128 on-shore water transport in the surface (0-40 m) layer and compensating offshore flow at
129 intermediate depths. For the Wandel Sea region adjacent to the tidewater glacier terminus, both
130 *Dmitrenko et al.* [2017] and *Kirillov et al.* [2017] reported on water properties modified by the
131 ocean-glacier interactions for depths exceeding 90-100 m. During summer (August 2015), the
132 glacier marine melt also affects the surface fresh water flux [*Bendtsen et al., 2017*].

133

134 **2. Data and methods**

135 The landfast ice-tethered oceanographic mooring was deployed over the southeast Wandel Sea
136 outer shelf at 81.768°N, 16.502°W from 15 May 2015 to 6 April 2016. The mooring was located
137 ~15 km from Station Nord, ~18-20 km from the landfast ice edge, and ~14 km from the tidewater
138 glacier terminus at 178 m depth at the glacial trough open to the continental slope (Figures 2b and
139 3). Deployment was conducted through 2.6 m thick multiyear landfast ice at a refrozen melt pond.
140 The mooring setup consisted of two Workhorse 300 kHz ADCPs placed at 3.3 m (down-looking)

141 and at 174 m (up-looking), two SBE-37 CT sensors by Sea Bird Electronics placed at 3.5 and 166
142 m, and an Ice Tethered Profiler (ITP) by McLane Research Laboratory preprogramed to cast every
143 3 hours in the depth range from 4.4 to ~150 m. The ITP was equipped with a CTD sensor 41CP
144 by Sea-Bird Electronics and Wetlabs ECO sensor for measuring backscatter intensity, chlorophyll
145 fluorescence and colored dissolved organic matter (CDOM) fluorescence for EX/EM = 370/460
146 nm. CTD and optical data were recorded approximately every 0.3 m and 1.5 m, respectively.
147 According to manufacturer specifications, the CTD sensor 41CP accuracy is $\pm 0.002^{\circ}\text{C}$, ± 0.002
148 salinity units and ± 2 dbar with a typical stability of 0.0002°C , 0.001 and 0.8 dbar per year,
149 respectively. The CDOM fluorometer was calibrated to quinine sulfate and had a sensitivity of
150 0.28 parts per billion (ppb). The SBE-37s data were used only for verifying the ITP CTD data. The
151 high-quality ITP CTD record is confirmed by observed agreement between the upper-/lowermost
152 ITP measurements at 4.4/150 m depth and the upper and lower SBE-37s at 3.5/160 m depth,
153 respectively. All sensors were calibrated by manufacturers prior to the expedition.

154 The velocity data were obtained at 2 m depth intervals, with a 30 min ensemble time
155 interval and 30 pings per ensemble. For the downward-looking ADCP the first measured bin was
156 located at 8 m depth (i.e., about 5 m below the ice), and ADCP measured the water layer down to
157 60-80 m depth. This ADCP stopped working on 26 December 2015, and there was a data gap from
158 7 July to 7 August 2015 when the ADCP transducer was blocked by a platelet ice layer (for more
159 details see *Kirillov et al.*, 2017). For the upward-looking ADCP the first bin was at 170 m depth,
160 and the ADCP sampled the water column up to 90-110 m depth. The RDI ADCPs precision and
161 resolution are $\pm 0.5\%$ and $\pm 0.1 \text{ cm s}^{-1}$, respectively. The compass accuracy was estimated to $\pm 8^{\circ}$
162 due to the small horizontal component of the Earth's magnetic field in the Wandel Sea (for more
163 details see *Kirillov et al.*, 2018). The measured current direction was corrected for the local
164 magnetic deviation ($\sim 18^{\circ}\text{W}$).

165 Mooring data were complemented by synoptic CTD surveys in April-May and August
166 2015 and April 2016. Between 17 April and 15 May 2015, 86 CTD profiles were collected from
167 the landfast sea ice (1.0 to 3.5 m thick) on the Wandel Sea shelf (*Dmitrenko et al.*, 2017 and Figure
168 3a). For this study we used only 16 profiles (i) taken east of the 17°30'W, (ii) exceeding 60 m
169 depth and (iii) located well away from the tidewater glacier terminus (Figures 3a and 4a-4c).
170 During 10-21 August 2015, 115 CTD casts were occupied over the ice-free area using inflatable
171 boats [*Bendtsen et al.*, 2017]. We use stations #155 and 159 taken on 21 August along the shore
172 side of the landfast ice edge (Figures 4a, 5d and 5e). These two stations were taken over the
173 southwestern rim of the glacier trough with depth exceeding 60 m, and close (~8-10 km) of the
174 mooring position. During 4-13 April 2016, 31 CTD profiles were taken from the landfast ice
175 primarily along the oceanographic section following the glacier trough and adjacent to the
176 tidewater glacier terminus. Here we use 8 profiles from the glacier trough and 3 profiles taken at
177 the semi-isolated glacier bay of ~2 km in diameter surrounded by the tidewater glacier terminus
178 (Figures 4b, 5f and 5g). The glacier profiles were selected to assess how ocean-glacier interactions
179 influence the Pacific-derived halostad. The CTD observations were carried out with a SBE-19plus
180 CTD that was calibrated by the manufacturer prior to the expedition, and was accurate to $\pm 0.005^{\circ}\text{C}$
181 and $\pm 0.0005 \text{ S/m}$.

182 Ice conditions over the Wandel Sea shelf, the adjoining fjords and the Greenland Sea
183 continental slope were monitored by MODIS (Moderate Resolution Imaging Spectroradiometer –
184 Figure 2b) and Sentinel-1 C-band SAR (C-Band Synthetic Aperture Radar) satellite imagery,
185 acquired daily by the Danish Meteorological Institute (<http://ocean.dmi.dk/arctic/nord.uk.php>). In
186 general, open water area, newly formed sea-ice, ice ridges, multiyear and first-year landfast sea
187 ice, refrozen leads, large icebergs and glacier terminations are distinguishable in SAR imagery.
188 Sea ice thickness was measured manually at each CTD station with an ice thickness tape. The 10-

189 m wind was obtained from the National Centers for Environmental Prediction (NCEP) – [Kalnay
190 *et al.*, 1996]. The horizontal resolution of the NCEP-derived wind is 2.5° latitude, and we used
191 time series of 10-m wind over the Wandel Sea continental slope at 82°N , 15°W . For the storm
192 event in 22-24 April 2015, Kirillov *et al.* [2017] reported on a relatively good agreement between
193 the winds derived from NCEP and from the Station Nord weather station.

194 The passive tracer analysis was carried out in a simulation of the Nucleus for European
195 Modeling of the Ocean (NEMO) version 3.4 [Madec and the NEMO team, 2008]. The Arctic and
196 the Northern Hemisphere Atlantic configuration, run at $1/12$ degree was used. The horizontal
197 resolution over the western Arctic is $\sim 4\text{-}5$ km. The sea ice module used here is the Louvain la-
198 Neuve Ice Model Version 2 with an elastic-viscous-plastic rheology [Hunke and Dukowicz, 1997],
199 including both thermodynamic and dynamic components [Fichefet and Maqueda, 1997]. The
200 model domain covers the Arctic and the Northern Hemisphere Atlantic with two open boundaries,
201 one close to Bering Strait in the Pacific Ocean and the other one at 20°S across the Atlantic Ocean.
202 Open boundary conditions (temperature, salinity and horizontal ocean velocities) are derived from
203 the monthly Global Ocean Reanalysis and Simulations produced by Mercator Ocean [Masina *et*
204 *al.*, 2017]. The simulation was integrated from January 1st 2002 to December 31 2016, driven with
205 high temporal (hourly) and spatial resolution (33 km) atmospheric forcing data provided by
206 Canadian Meteorological Centre Global Deterministic Prediction System ReForecasts dataset
207 [Smith *et al.*, 2014]. There is no salinity restoring. Further details, as well as model evaluation, can
208 be found in Hu *et al.* [2018] and Courtois *et al.* [2017]. The passive tracer is introduced into the
209 model at the Bering Strait, starting from the beginning of the model experiment on January 1,
210 2002. The amount of tracer input is proportional to the flux in each grid cell at the Bering Strait.
211 Thus the tracer flux replicated the seasonal and inter-annual variability of the Bering Strait inflow.

212 For the Wandel Sea continental slope and outer shelf fields are presented as depth integrated
213 through the 20-85 m depth layer roughly associated with Pacific-derived halostad.

214

215 **3. Results**

216 **3.1. CTD survey in April-May 2015**

217 The water mass description for the southeast Wandel Sea shelf made by *Dmitrenko et al.* [2017]
218 based on CTD profiles occupied in April-May 2015 assigned a halostad layer from about 15 m to
219 65 m depth to Pacific-derived water. This interpretation is based on similarities between the
220 Wandel Sea halostad and the cold halostad of Pacific origin identified in the Canada Basin by
221 *Shimada et al.* [2005]. The halostad layer in the Wandel Sea is characterised by weak vertical
222 salinity difference (salinity 30 to 31.2-31.5) and water near the freezing point (*Dmitrenko et al.*,
223 2017; in Figure 5 the halostad is highlighted with blue shading). At the top, the subsurface
224 halocline layer with a strong vertical salinity gradient (salinity 1 m^{-1}) separates the halostad from
225 the relatively fresh (salinity of 16–21, not shown) surface layer of local origin comprised of
226 summer snow and sea-ice meltwater [*Kirillov et al.*, 2018] and freshwater from the glacial runoff
227 [*Bendtsen et al.*, 2017]. At the bottom, the halostad is limited by the Atlantic-derived thermocline
228 and halocline with salinity centered between 32.5 and 33 and temperatures steadily increasing with
229 depth up to $>0^{\circ}\text{C}$ in the Atlantic layer at depths exceeding 140 m [*Dmitrenko et al.*, 2017]. In
230 Figure 5 the Atlantic-derived halocline is highlighted with pink shading.

231 A more detailed view on the Wandel Sea halostad in April-May 2015 reveals that over the
232 southeast shelf area covered with CTD data and limited to about 25 x 25 km (Figure 3), the halostad
233 shows significant spatial variability with depths of its lower boundary varying from 55 m to 77 m
234 (overlapping between blue and pink shading in Figures 5a and 5b). In fact, the halostad shows two

235 different modes that results in a splitting of the Atlantic-derived halocline for both temperature
236 and salinity profiles through the 50-100 m depth range (Figures 5a and 5c). On average, the deep
237 mode of the halostad is ~12-15 m deeper than the shallow mode (blue and red profiles in Figure
238 5a and 5b, respectively). The depths of the halocline change accordingly (Figures 5a and 5b). At
239 the base of the deep halostad mode from 65 m to 77 m depth, water is cooler by ~0.15°C (Figure
240 5a) and fresher by ~0.7 (Figure 5c) than the shallow mode.

241 The spatial analysis assesses the main patterns of the deep and shallow halostad and relates
242 them to their geographical location on the southeast Wandel Sea shelf area covered with CTD data.
243 A deep halostad with a base comprised by cooler and fresher water occupies the deeper glacier
244 trough and extends over its eastern flank open to the Wandel Sea continental slope (blue dots in
245 Figure 3). The minimal water temperature -1.73°C at the base of the halostad at 70 m depth was
246 observed at station 65, i.e. the station closest to the Wandel Sea continental slope (Figures 3 and
247 5a). In contrast, a shallow halostad is recorded in the middle of the glacial trough and its flanks
248 (red dots in Figure 3). Note that CTDs occupied at proximity to the tidewater glacier terminus were
249 excluded from this analysis (Figure 3) due to the ocean-glacier modifications imposed at the base
250 of the halostad [Dmitrenko *et al.*, 2017]. However, we will address this point below in section 3.3
251 discussing CTD data from April 2016. All other stations involved in our analysis represent the
252 transition from a deep to shallow halostad. They occupy the western flank of the glacier trough
253 open to the Wandel Sea mid-shelf area (green dots in Figure 3 and green lines in Figures 5a-5c).

254 Overall, over a rather limited area in the southeast Wandel Sea shelf, we detect two
255 different halostad modes clearly showing spatial regularities. In the following we refer to a deep
256 (cooler and fresher) mode as the “winter” mode, and a shallow (warmer and saltier) mode as the
257 “summer” mode. This attribution is primarily based on the thermohaline properties at the base of

258 the halostad showing spatial regularities over the southeast Wandel Sea shelf. In the following,
259 however, we will link these spatial features to seasonal variability.

260 **3.2. CTD survey in August 2015**

261 Two CTD casts used for this study were taken on 20-21 August 2015 from the open water near the
262 interior landfast ice edge over the western flank of the glacier trough (Figure 4a). In terms of the
263 halostad, these CTD casts closely resemble the summer mode of April-May 2015 (Figures 5a-5e).
264 The base of the halostad at ~40 m depth (~10-15 m shallower comparing to April-May) shows a
265 minimum temperature of -1.66°C at a salinity of 31.3, and this is $\sim 0.02^{\circ}\text{C}$ warmer and 0.25 saltier
266 comparing to April-May. At its upper boundary (15 m depth), the August halostad was found to
267 be $\sim 0.3^{\circ}\text{C}$ warmer and 0.25 saltier, i.e. the same salinity anomaly as observed at the lower
268 boundary. Thus, seasonal freshening expected through the upper water layer due to fresh water
269 flux from snow, sea-ice and glacier melt was not observed. The most significant changes, however,
270 occurred over the central part of the glacier trough (dashed lines in Figures 5d and 5e). Based on
271 moored CTD data, the halostad has been shallowed from 68 m to ~50 m depth. The associated
272 changes in temperature and salinity at 50 m depth are recorded to $\sim 0.02^{\circ}\text{C}$ and 0.3, respectively,
273 showing similar tendencies as over the western flank of the glacier trough. At 15 m depth, the
274 glacier trough halostad was warmer and saltier by $\sim 0.13^{\circ}\text{C}$ and 1.0, respectively, relative to April-
275 May.

276 Overall, the general assessment of the halostad variability from April-May to August is
277 that the summer mode expanded from the mid-trough to the western flank and mooring position
278 substituting the transitional and winter mode. However, the increase in salinity through the upper
279 halostad at the mooring location (~ 1) is unlikely to be explained by alternating from winter to

280 summer mode. For April-May 2015 at 15 m depth the summer mode salinity exceeds salinity at
281 mooring position only by ~ 0.3 .

282 3.3. CTD survey in April 2016

283 CTD profiles taken in 4-8 April 2016 along the glacier trough show only the winter mode of the
284 halostad (Figures 4b, 5f and 5g). In April 2016, no CTD stations were taken over the western flank
285 of the glacier trough, and the summer mode was likely therefore not sampled. The halostad was
286 recorded ~ 7 m shallower, 0.4°C cooler and 0.8 saltier comparing to April-May 2015. Thus, if the
287 seasonal cycle occurs through the Pacific-derived halostad, then it is not closed due to salt influx
288 observed from 2015 to 2016. This tendency is also evident from CTD profiles carried out in August
289 2015 (Figures 5d and 5e). As of April-May 2015, the minimal temperature (-1.73°C) was recorded
290 at the base of the halostad at ~ 60 m depth (Figure 5f).

291 CTD profiles occupied in April 2016 at the semi-isolated glacier bay surrounded by the
292 tidewater glacier terminus (purple dots in Figure 4b) show the potential of the tidewater outlet
293 glacier for modifying water properties through the Atlantic-derived halocline. These three CTD
294 profiles, grouped into the halostad glacier mode, show exceptionally low water temperatures down
295 to -1.79°C through 63-85 m depth (purple lines in Figure 5f). As a result, the upper 20-m portion
296 of the halocline does not show a temperature increase with depth, as typical for profiles comprising
297 summer and winter modes of the halostad (Figures 5a-5e).

298 Based only on temperature profiles, one may suggest that the purple profiles in Figure 5f
299 represent the winter halostad deepened down to ~ 85 m. However, the corresponding salinity
300 profiles through this depth range are not modified accordingly and look similar to those taken over
301 the glacier trough ~ 5 - 10 km from the tidewater glacier terminus (Figure 5g). Thus, the relative

302 cold temperatures can only be explained only if the upper portion of the halocline was thermally
303 modified without freshening involved, i.e. cooled by glacier ice.

304 Water cools when it comes in contact with glacier ice that is colder than the in situ freezing
305 point of sea-water. So, the glacier-ocean interaction does not necessarily involve freshening, if sea-
306 water temperature is below the in situ freezing point of the glacier ice. The glacier mode profiles
307 in Figure 5f represent an example of the glacier-ocean thermal interaction without significant
308 glacier melt contribution. Note, however, that all CTD profiles taken in 2015-2017 from the
309 landfast ice at the vicinity of the tidewater glacier terminus, show cooler and fresher water below
310 100 m depth compared to ambient profiles taken well away from the glacier terminus (not shown).
311 Moreover, the mooring optical data of CDOM fluorescence presented below (section 3.4.2) allows
312 to differentiate the Pacific-derived halostad from the glacier-modified halocline.

313 **3.4. Mooring data from May 2015 to April 2016**

314 **3.4.1. ADCP Velocity data**

315 For this research we use velocity data from 8, 50 and 160 m depth. The velocity time series at 8 m
316 is from the uppermost down-looking ADCP bin and indicates the under-ice water dynamics. The
317 50 m depth velocities are intended to describe the halostad water dynamics and derived from the
318 deepest bin of the ice-tethered downward-looking ADCP. During winter the profiling range was
319 significantly reduced due to insufficient scattering in the water column, and the base of the halostad
320 at ~50 to 75 m depth is unresolved with velocity data. ADCP data at 160 m, well below the depth
321 of the 0° isotherm separating the Atlantic Water layer from the from the upper layers (~140 m
322 depth, *Dmitrenko et al.*, 2017), describes the Atlantic water layer dynamics.

323 Figure 6 shows a progressive vector diagram based on the 24-h mean ADCP velocity time
324 series for each selected depth. From the mooring deployment on 16 May 2015 (Julian day JD136)

325 to 5 August (JD217), the sub-ice water layer shows insignificant water transport (Figure 6a) with
326 a mean speed of $0.3 \pm 1.4 \text{ cm s}^{-1}$ to the east (90°). Following JD217 and until 16 October (JD289),
327 a northeast flow aligned to $\sim 70^\circ$ was observed with a mean velocity $4.0 \pm 3.1 \text{ cm s}^{-1}$. During this
328 time the hypothetical water parcel can be transported by $\sim 25 \text{ km}$ from the source region located
329 over the western flank of the glacier trough. Based on the satellite imagery, the one-year old
330 landfast ice was rapidly retreating from this area since 16 August 2015 (not shown), and on 19
331 August the region was already ice free (Figure 4a). The northeastward shelf outflow was
332 interrupted from 21 August to 7 September (JD233-250) and modified during events I (25
333 September – 3 October, JD268-276) and II (7-16 October, JD280-289) – Figure 6a. After 20
334 November (JD324), the northeast water transport was restored and dominated until the end of
335 ADCP record (24 December 2015, JD358).

336 In contrast to the sub-ice water layer, the halostad at 50 m depth shows an on-shelf flow
337 aligned to 237° at $3.7 \pm 2.8 \text{ cm s}^{-1}$ from the day of deployment to 15 June (JD136-JD166) – Figure
338 6b. During this inflow event, the hypothetical water parcel can be potentially transported by ~ 100
339 km from the area located over the Wandel Sea continental slope crossing the Wandel Sea outer
340 shelf to the mooring location (note that the mooring was deployed $\sim 20 \text{ km}$ from the Wandel Sea
341 shelfbreak). Afterwards, the down-looking ADCP transducer was blocked by the platelet ice layer
342 until 2 August (JD214), and no significant dynamics was recorded to 7 September (JD250) –
343 Figure 6b. Since that time, a consistent shelf outflow of $\sim 2.0 \pm 1.8 \text{ cm s}^{-1}$ aligned to 68° was
344 recorded almost until the end of the record. In fact, this flow was exactly in opposite direction to
345 the shelf inflow observed for JD136-166 (Figure 6b). This outflow, however, was reversed for 1-
346 17 November (JD305-321) and modified during events I and II, similarly to the 8 m depth level
347 (Figures 6a and 6b). However, the direction was more aligned to the south during the initial phase
348 of disturbance that seems to be in accordance with the Ekman spiral responding to wind forcing.

349 For the Atlantic water layer at 160 m depth, the period after deployment to 17 July (JD198)
350 is characterised by weak water dynamics without sustainable water transport, similar to the sub-
351 ice water layer. Afterwards, an on-shelf inflow aligned to 138° at $0.8 \pm 0.6 \text{ cm s}^{-1}$ was observed
352 until 11 September (JD254) – Figure 6c. This flow direction corresponds to the orientation of the
353 glacier trough open to the Wandel Sea continental slope in $\sim 55 \text{ km}$ to the northeast from mooring
354 position (Figures 2b and 3a). From JD198 to JD254, the hypothetical water parcel can be
355 transported along the glacier trough by $\sim 40 \text{ km}$ (Figure 6c), and on the mid of September 2015 the
356 water sampled by the mooring can originate from the Wandel Sea continental slope. The along-
357 trough water inflow was interrupted from 12 September to 15 October (JD255-288), particularly
358 by events I and II, but then continued to 164° with a speed of $0.6 \pm 0.4 \text{ cm s}^{-1}$ to 28 October (JD301).
359 Afterwards, until mooring recovery on 6 April 2016 (JD462), no sustainable water flow was
360 recorded (Figure 6c).

361 **3.4.2. ITP CTD and CDOM data**

362 Figures 7b, 7c and 7d show the year-long measurements of temperature, salinity and CDOM
363 fluorescence, respectively, from the landfast ice-tethered ITP profiler. Before going into details,
364 we point out that the entire ITP record shows the halostad enriched with CDOM, as was reported
365 by *Dmitrenko et al.* [2017] for the short-term mooring deployed at the front of tidewater glacier
366 terminus in April 2015. The CDOM temporal variability reflects the structure of the halostad and
367 underlying halocline from ~ 15 to 90 m depth (Figure 7). The sub-surface melt water layer with
368 salinity < 25 and Atlantic water layer with salinity > 34.5 below $130\text{-}140 \text{ m}$ depth have a lesser
369 CDOM content ($< 80 \text{ ppb}$).

370 Based on tendencies of CTD and CDOM fluorescence, we conventionally subdivided the
371 entire mooring record to the (i) relatively stable period to the end of June ($\sim \text{JD}180$), (ii) transition

372 period from the end of June to the end of October (~JD300), (iii) relaxation period from the end
373 of October to February (~JD420), and again (iv) the relatively stable period from the end of
374 February to the end of record in April 2016 – Figure 7 bottom. Below we focus on each period,
375 also putting them in a context of water dynamics (Figures 6 and 7a) and the regional CTD surveys
376 carried out in April-May and August 2015, and April 2016 (Figure 5).

377 During the stable period in May-June 2015, no significant variability was observed, while
378 the boundary between the halostad and halocline was slightly shallowed by ~8 m (Figures 7b and
379 7c). It was accompanied by reduction of CDOM fluorescence at the low and upper boundaries of
380 the halostad from ~107-108 to 105 ppb, and through the halocline from 107 to 90 ppb (Figure 7d).
381 The under-ice water layer at 5-10 m depth and Atlantic water layer below 140 m depth remain
382 relatively stable (Figures 7b-7d). Note that during this period the on-shelf inflow was observed in
383 the halostad (Figure 7a).

384 The transition period is characterized by the northeastward shelf outflow for the sub-ice (8
385 m depth) and halostad (50 m depth) layers and inflow for the Atlantic water (160 m) along the
386 glacier trough (Figures 6 and 7a). This was accompanied by significant modifications through the
387 entire water column (Figures 7b-7d). The under-ice 10-m thick water layer shows warming (up to
388 ~2.5°C) and freshening (down to 17-20) attributed first to a drainage of snow meltwater through
389 the landfast ice (JD196-216) and then to a pulse of warm meltwater advected from the ice-free
390 area generated over the western flank of the glacier trough to southwest of mooring location
391 (JD226-247, Figures 4) - *Kirillov et al.* [2018]. This is confirmed by the velocity time series at 8
392 m depth showing consistent northeastward flow starting JD218 (Figures 6a and 7a). For the deeper
393 layer below 10 m depth, the halostad, halocline and underlying Atlantic water layer were elevated
394 up to 20 m as follows. The temperature and salinity time series show gradual shallowing of the
395 halostad lower boundary from ~65-70 m depth in May-June 2015 to ~35-40 m depth to the mid-

396 September (Figures 6b and 6c). During this time, at 65 m depth salinity increased from ~31.50 to
397 33.15 (Figure 7c) accompanied by warming from ~-1.7°C to -1.45°C (Figure 7b). At 35 m depth
398 salinity increased from 30.8 to 31.6 while remaining at almost constant temperature. At the top of
399 the halostad (~15 m depth) salinity increased from 30 to 30.8 and temperature raised by ~0.2°C.
400 The shallowing of the halostad was accompanied by a corresponding shallowing of the Atlantic
401 water layer traced by the 0°C isotherm. From the end of June to mid-September, the 0°C isotherm
402 shallowed from 145-150 m to 125-130 m (Figure 7b), and the isohaline 34.5 was correspondingly
403 uplifted by ~20 m (Figure 7c).

404 During the transition period, the CDOM concentration was significantly lowered through
405 the entire water layer sampled by the ITP (Figure 7d). Through the halostad and underlying
406 halocline, CDOM was reduced from ~105-107 to 95-100 ppb and from 105 to 85-90 ppb,
407 respectively. The CDOM reduction in the sub-ice water layer was similar to halocline. In the
408 Atlantic Water layer, CDOM was lowered from ~80-85 to 70-75 ppb.

409 As of synoptic variability at ~8-10-day time-scale, events I and II identified at the end of
410 the transition period, based on velocity data (red-dashed rectangular in Figure 7), represent the
411 most significant disturbances of the CTD and CDOM general tendencies. Both events show similar
412 CTD and CDOM structure: saltier, cooler and less CDOM water at the upper halostad from the
413 beginning of the events followed by fresher, cooler and high CDOM water at the low halostad. We
414 also note that for the halostad the mooring time series for the transition period are consistent with
415 modification of CTD profiles from April-May to the end of August based on the areal CTD survey
416 (Figures 5a-5e). Both the CTD casts and ITP data shows salinification throughout the entire
417 halostad layer, while a freshening tendency from winter to summer can be expected due to snow,
418 ice and glacier melt as observed for the sub-ice water layer where salinity decreased from >25 in
419 May-June to 17-20 in August-October (Figures 7b and 7c).

420 The relaxation period is characterized by a gradual return to the initial CTD conditions of
421 May-June 2015 (Figures 7b and 7c) after termination of the Atlantic water on-shelf flow at the end
422 of October 2015 (Figures 6c and 7a). The under-ice water layer cools down to $\sim 1^{\circ}\text{C}$ at salinity
423 ~ 25 . The lower boundary of the halostad and the halocline water layer were deepened to about the
424 same depth as of May-June 2015. This tendency is obvious since JD370 when the low part of
425 halostad at 70 m depth started to cool down to -1.75°C and freshened by ~ 1 . At this time, CDOM
426 showed a gradual reduction through the upper halostad, and only the low halostad maintained the
427 CDOM values typical for the end of transition period.

428 The stable period in February-April 2016 is different from that in May-June 2015 by higher
429 salinity (by ~ 0.5) and lower CDOM (by ~ 7 ppb). For example, during the first ten days of March
430 2016 at 60 m depth, the lower halocline was saltier by ~ 0.4 , but almost at the same temperature
431 ($\sim 1.7^{\circ}\text{C}$) as in May 2015. This result is consistent with CTD profiles taken along the glacier trough
432 in April 2016. Overall, from May 2015 to April 2016 the halostad became saltier, but less in
433 CDOM that suggests a relationship between salinity and CDOM through the halostad depth range.

434 The TS scatterplots of the temperature, salinity and CDOM time series from ITP shows
435 seasonal evolution of the CDOM maxima in the *TS* space (Figure 8). From the stable to transitional
436 period, the CDOM maxima became saltier (by ~ 1) and denser (by $\sim 0.5 \text{ kg m}^{-3}$) – Figures 8a and
437 8b. During the relaxation period, a gradual return to the initial thermohaline conditions of the
438 CDOM maxima is observed (Figures 8c and 8d), but the CDOM values are reduced by ~ 10 ppb
439 (Figures 7 and 8).

440 Overall, the results derived from the ITP data for depths exceeding 15 m are consistent
441 with a seasonal cycle observed through the halostad and underlying Atlantic water layer over the
442 southeastern Wandel Sea shelf. From May to October, the lower boundary of the halostad is

443 shallower, and the halostad is warmer, saltier and has a lower CDOM concentration. We refer to
444 this pattern as the halostad summer mode. We also recorded that the halostad was consistent with
445 the summer mode in April-May 2015 over the western flank of the glacier trough. During
446 “summer”, the Atlantic water layer is elevated, warmer and saltier. In contrast, from January to
447 May, the low boundary of halostad is deepened, and the halostad is cooler, fresher, and the CDOM
448 is enriched. We refer to this modification as the halostad winter mode. The halostad consistent
449 with winter mode was revealed in April-May 2015 and April 2016 over the glacier trough at a
450 distance of the tidewater glacier terminus. During “winter”, the Atlantic water layer is deeper,
451 cooler and less saline. In general, the summer mode is associated with on-shelf inflow of the
452 Atlantic water, and outflow of the overlaying halostad water. In contrast, the winter mode is related
453 to the on-shelf inflow of the halostad water.

454

455 **4. Discussion**

456 **4.1. Assessment of the seasonal cycle based on areal data and mooring observations**

457 We suggest that the seasonality in water column properties in the southeast Wandel Sea below the
458 under-ice meltwater layer is generated by the lateral displacement of the coastal branch of the PW
459 outflow from the Arctic Ocean to the western Fram Strait driven by the annual cycle in wind
460 forcing observed over the Wandel Sea continental slope. Seasonality of the solar radiation has little
461 influence on the intermediate water layer, which is isolated year-round from the surface by the
462 sub-surface halocline with exceptionally strong salinity (density) stratification [*Bendtsen et al.*,
463 2017; *Dmitrenko et al.*, 2017; *Kirillov et al.*, 2018]. Further indication of its isolation from the
464 surface water is that during summer the water layer below 15 m depth exhibits salinification, while
465 freshening is expected due to snow, sea-ice and glacier melt. This is most likely due to advection

466 of the seasonal signal from upstream with the Pacific-derived Arctic water flow along the
467 Greenland coast.

468 Following *Dmitrenko et al.* [2017], we attribute the Wandel Sea halostad layer to the
469 Pacific-derived Arctic water. For 2008-2009 over the upstream Lincoln Sea area (Figure 1), *de*
470 *Steur et al.* [2013] reported on PW at 32.5-33.5 salinity as cold as -1.65°C . In the Canada Basin,
471 the cold halocline with temperatures down to -1.5°C at salinities of $\sim 32-33$, originating from the
472 Chukchi Sea shelf [*Timmermans et al.*, 2017], is likely comprised by the Pacific winter water.
473 Over the western (Alaskan) Beaufort Sea, water with the salinity $31 < S < 33$ is generally assigned
474 to PW [*von Appen and Pickart*, 2012]. This definition is also applicable for the eastern (Canadian)
475 Beaufort Sea [*Dmitrenko et al.*, 2017]. The haline properties of the Wandel Sea halostad are
476 generally in line with these definitions (Figure 8). They are also consistent with ~ 32.2 salinity of
477 the Pacific-derived Arctic water in Fram Strait reported by *Jones et al.* [2003]. However, the
478 salinity of the Wandel Sea upper halostad ($\sim 20-25$ m depth) of ~ 30 is too low to be assigned to
479 PW. Moreover, the temperature of the Wandel Sea lower halostad ($\sim 60-70$ m depth) of -1.75°C is
480 too low to be assigned to the Pacific Winter water. Thus, PW has been modified en route through
481 the Arctic Ocean to northwest Fram Strait. The low salinity shelf water from the Siberian shelves
482 modifies PW either across the Chukchi Sea or crossing over the Lomonosov Ridge into the
483 Makarov Basin and eventually entering the Canada Basin [*Morison et al.*, 2012]. The lower
484 halostad temperature close to the freezing implies that PW has been recently ventilated from the
485 surface during winter en route to the Wandel Sea. This also confirms the remote origin of the
486 halostad. The southeastern Wandel Sea shelf is landfast ice covered and stratified all year around
487 preventing ventilation of the water column locally [*Dmitrenko et al.*, 2017; *Bendtsen et al.*, 2017].

488 The Pacific origin of the Wandel Sea halostad is also confirmed by the elevated values of
489 the CDOM fluorescence (Figure 7c). CDOM in the Arctic originates predominantly from

490 terrigenous organic matter primarily attributed to the Eurasian and American continental runoff
491 water [Amon *et al.*, 2003; Stedmon *et al.*, 2011] as well as to interactions with sediments on the
492 Arctic shelves [Guéguen *et al.*, 2007; Stedmon *et al.*, 2001]. The CDOM fluorescence maxima in
493 the halostad is consistent with results from the Canada Basin where this maxima is attributed to
494 the PW of winter origin [Guéguen *et al.*, 2007] and the continental river runoff water [e.g.,
495 Granskog *et al.*, 2012]. For the downstream NEW area, Amon *et al.* [2003]) reported the two
496 intermediate maxima of the CDOM fluorescence: through the shelf halostad layer and continental
497 slope at salinities of ~32.0-32.5 and ~33.0-33.5, respectively, and temperature of ~-1.7°C (see also
498 Falck, 2001). This could be a differentiation between the PW CDOM and CDOM from the
499 Siberian Rivers. The NEW shelf maximum resembles the TS characteristics of the CDOM
500 maximum in the Wandel Sea (Figure 8).

501 The CDOM over the Wandel Sea shelf shows the seasonal patterns consistent with those
502 for temperature and salinity (Figures 7 and 8). During “summer”, the reduced CDOM maximum
503 is associated with saltier (by ~1), denser (by ~0.5 kg m⁻³) and shallower water layer (Figures 7, 8b
504 and 8c). In context of the results by Amon *et al.* [2003], we speculate that the “winter” CDOM
505 maxima in the lower halostad (Figures 8a and 8d) is likely from the PW passage over the Chucki
506 Sea shelf than the Siberian river runoff passage with Transpolar Drift.

507 What causes the seasonal-like behavior of the Pacific-derived halostad? PW in the Arctic
508 Ocean clearly shows seasonality. There are strong seasonal variations in the thermohaline signal
509 upstream in the Bering Strait where PW inflows to the Arctic Ocean [Woodgate *et al.*, 2005, 2012].
510 Over the Chukchi and western Beaufort seas, PW shows summer and winter mode based on its
511 formation. The summer PW with temperatures above -1.2°C and salinities between 31 and 32
512 [Steele *et al.*, 2004], is usually comprised of the Chukchi Summer Water [Woodgate *et al.*, 2005]
513 and the Alaskan Coastal Water [Pickart *et al.*, 2005]. Below the summer PW is a layer of winter

514 PW that can be as cold as -1.45°C and forms during winter sea-ice formation within the Bering
515 and Chukchi shelves [*Jones and Anderson, 1986; Weingartner et al., 1998; Pickart et al., 2005*].
516 The advection of the Pacific winter water is also tied to seasonality of the Bering Strait inflow to
517 the Arctic Ocean [*Shroyer and Pickart, 2018*]. Overall, it should come as no surprise that a
518 seasonal modulation of the PW properties can occur downstream over the Canada Basin and
519 Canadian Beaufort Sea. For example, the seasonal signal in the Arctic Ocean AW boundary current
520 at depths exceeding 180-200 m maintains its identity along the Nansen Basin Siberian margin
521 ~ 2500 km downstream from the source area in eastern Fram Strait [*Dmitrenko et al., 2009*]. For
522 the Canada Basin using the year-long CTD record (2009-2010) from the drifting ITP, *Timmermans*
523 *et al.* [2017] reported on the seasonal cycle through the halocline layer, which is consistent with
524 that recorded by our mooring in the Wandel Sea. However, the cold halocline in the Canada Basin
525 with temperatures of -1.5°C to -1.75°C was found deeper (110-230 m depth) comparing to the
526 Wandel Sea. The PW seasonal modulation can be expressed as alternation between summer and
527 winter PW that is, in general, consistent with alternation between summer and winter modes of the
528 Wandel Sea halostad. It is possible, however, that the observed seasonal changes over the southeast
529 Wandel Sea shelf are instead governed by a wind-driven seasonal shift of the PW boundary current
530 relative to the shelfbreak, as was described for the AW boundary current along the Siberian
531 continental slope by *Dmitrenko et al.* [2006].

532 For duration of field operations at SN in 2015-2016, the time series of the 24-h mean wind
533 were generated using the NCEP data set (Figures 9a and 9b). Zonal and meridional 10-m wind
534 data were derived for the Wandel Sea continental slope ~ 35 km from the mooring (Figures 2a, 4a,
535 9c and 9d). In general, the landfast ice cover eliminates the surface wind stress. However, for the
536 landfast ice-covered areas over the Greenland coast in ~ 20 -50 km to the landfast ice edge, the

537 wind-forced circulation can be induced by upwelling and downwelling developed at the vicinity
538 of the landfast ice edge [*Dmitrenko et al.*, 2015; *Kirillov et al.*, 2017].

539 It seems that the on-shelf inflow of the halostad water is controlled by the downwelling-
540 favourable northerly winds. The storm event driven by northerly winds up to 15 m s^{-1} occurred in
541 the third ten-day period of April 2015 (JD112-114, Figures 9a and 9b). The short-term mooring
542 deployed at the front of tidewater glacier terminus recorded the on-shelf inflow through the water
543 layer down to $\sim 50 \text{ m}$ depth and outflow in the layer beneath, which is consistent with downwelling
544 [*Kirillov et al.*, 2017]. Before 30 May 2015 (JD150), the ADCP velocity data from 50 m depth
545 (Figure 6b) show relatively weak on-shelf inflow with a mean velocity of 2.2 cm s^{-1} . In contrast,
546 during the following 6 days the on-shore transport increased more than twice up to 5.2 cm s^{-1} . This
547 enhancement is clearly attributed to the northerly wind events during JD151-156 (Figure 9b). Note,
548 however, that since May 2015 the mean atmospheric forcing changed to the upwelling-favourable
549 southerly winds dominated to the mid-October 2015 (Figure 9b).

550 For the upwelling-favourable wind forcing, the AW on-shelf inflow is expected along with
551 outflow through the overlaying halostad and under-ice water layers. In fact, the on-shelf AW flow
552 along the glacier trough was observed lagging the upwelling-favourable storms in JD170-190 by
553 about one month (Figure 8b). We speculate that this delay is attributed to the landfast ice extending
554 eastward beyond the shelfbreak suggesting that upwellings are sensitive to the sea-ice conditions
555 over the continental slope. The Wandel Sea is the only place in the high Arctic where the landfast
556 ice can extend over the shelfbreak and upper continental slope. The satellite imagery shows that
557 since mid-December 2014 the landfast ice edge, controlled by northerly winds through a surface
558 Ekman onshore transport, was gradually extending eastward (not shown) and in mid-March 2015
559 it was finally stabilized over the Wandel Sea upper continental slope (e.g., Figure 9c). On 13 July
560 2015 (JD194) the outer part of the landfast ice area was collapsed, and the landfast ice edge was

561 resided onshore by ~17 km beyond the shelf break (Figure 8). Five days later starting 17 July
562 (JD198), the AW on-shelf flow was established in response to the upwelling-favourable southerly
563 wind forcing. This is consistent with results by *Carmack and Chapman* [2003]. Based on
564 numerical simulations of shelf-basin exchange, they reported on abrupt onset of the shelfbreak
565 upwelling when the ice edge retreats beyond the shelfbreak.

566 From the end of October 2015 to the end of the mooring record in April 2016, the
567 atmospheric forcing was again dominated by the downwelling-favourable northerly winds (Figure
568 9b). For the downwelling-favourable storms in November 2015 (JD311-322), the outflow at 50 m
569 depth was reversed to westward direction, which is more consistent with on-shelf inflow driven
570 by downwelling. However, later on the northeast flow was retained, while northwestward flow is
571 expected to continue as far as the downwelling-favourable wind forcing is imposed, i.e. until the
572 end of February 2016 (Figure 9b). We are unable to evaluate the halostad water dynamics after 26
573 December 2015 when the ice-tethered ADCP stopped working. However, we note that as soon as
574 southerly winds over the Wandel Sea continental slope were reversed on ~JD300, the AW inflow
575 along the glacier through was terminated.

576 To evaluate in more details the response of the water column to wind forcing, we
577 specifically focused on four upwelling-favourable storms in September-October 2015 (#I and II),
578 and during the end of December 2015 (#3) and mid-March 2016 (#4). Among these four storms,
579 #III and IV were strongest, with maximal southerly winds up to 10.0 m s^{-1} (29 December 2015,
580 JD363) and 11.2 m s^{-1} (11 March 2016, JD436), respectively – Figures 9b and 10b-f. For storms
581 in September-October 2015, the upwelling-favourable southerly wind forced the pack ice off the
582 landfast ice edge, and a polynya was developed over the upper continental slope (Figures 10a-d).
583 This wind, however, was reversed, lagging southerly wind maximums by 2-4 days (Figure 9b).
584 For storm events in December 2015 and March 2016, the landfast ice was recorded extending over

585 the Wandel Sea continental slope, and it was not extensively modified during storms (Figures 10e
586 and 10f).

587 Events III and IV show no significant CTD and CDOM variability that can be attributed to
588 wind forcing (Figure 7). As of our preceding discussion on the delay of upwelling onset in response
589 to summer upwelling-favourable wind forcing, we attribute this to the landfast ice extension over
590 the upper continental slope (Figures 10e and 10f). In contrast, events I and II show significant
591 modifications in response to wind forcing in a similar way for both events. From the beginning,
592 through the upper halostad layer (~15-45 m depth) the CDOM was lowered by ~8-10, and salinity
593 increased by ~0.2. This is consistent with east-southeastward transport (Figures 6a and 6b) of the
594 mid-shelf water less affected by the Pacific-derived Arctic water. In ~4-5 days following this
595 modification, at the lower depths (70-90 m) water became fresher (by ~0.3), cooler (by 0.2-0.4°C)
596 and higher in CDOM (by ~5) – Figure 7. This is consistent with deepening of the halostad in
597 response to the downwelling-favourable northerly winds lagging behind the upwelling-favourable
598 wind forcing by ~2-4 days.

599 Following *Dmitrenko et al.* [2017], we assume that the source of the halostad water is
600 located over the Wandel Sea shelfbreak and upper continental slope, i.e. the area of the coastal
601 branch of the Pacific-derived Arctic water. To confirm the source of the halostad water we use the
602 3-D CTD/CDOM-winds and CTD/CDOM-currents scatter analysis carried out using mooring-
603 derived ITP and ADCP data at 50 m depth and NCEP-derived 10-m wind over the Wandel Sea
604 continental slope – Figure 11. The scatter plots for wind (Figure 11d) and current (Figure 11h)
605 illustrate confidence of the scatter analysis in Figures 11a-c and 11e-g for variety of winds and
606 currents. Scatter analysis of temperature, salinity, CDOM records and wind shows that
607 southeasterly along-slope winds are generally associated with lower temperatures, lower salinity
608 and higher CDOM at the mooring location. This is consistent with on-shelf Ekman transport of

609 these anomalies from the continental slope. In contrast, the northwesterly winds are attributed to
610 warmer, saltier and less CDOM-rich water assuming the off-shelf Ekman transport originated from
611 the Wandel Sea mid-shelf (Figures 11a-c). The average rate of temperature, salinity and CDOM
612 anomalies related to change in wind patterns is estimated at $\pm 0.15^{\circ}\text{C}$, ± 0.2 and ± 2 ppb,
613 respectively. Scatter analysis of temperature, salinity, and CDOM records versus currents clearly
614 indicate the source of anomalies recorded by mooring (Figures 11e-g). The northeastward flow
615 carries warmer, saltier and less CDOM water from the mid-shelf. The southeastward flow transports
616 cooler, fresher and CDOM enriched water from the shelfbreak. The associated mean anomalies of
617 temperature, salinity and CDOM are similar to those driven by wind (Figures 11e-g).

618 The general assessment of wind forcing, water dynamics, CTD areal survey data and CTD
619 and CDOM mooring data explains the spatial and temporal variability of the halostad water layer
620 over the southeast Wandel Sea shelf. During winter, the northerly downwelling-favourable winds
621 force the halostad water to flow on-shelf, comprising the winter mode of the Pacific-derived
622 halostad over the Wandel Sea outer shelf (Figures 6b, 7 and 8b). The southerly upwelling-
623 favourable winds in July-October induce shelf outflow through the halostad water layers (Figures
624 6a, 6b and 9b). For the sub-surface layer, the northeast flow in August-October favours transport
625 of a relatively warm melt water from the ice-free area to the outer shelf covered by multiyear
626 landfast ice [Kirillov *et al.*, 2017]. It is confirmed by mooring CTD and velocity data (Figures 6a
627 and 7). During this time the halostad winter mode was subsidised with summer mode recorded in
628 April-May 2015 to the southeast of our mooring (Figures 5a-5e) suggesting lateral off-shore
629 displacement of the winter halostad in response to upwelling. The upwelling of modified AW
630 along the glacier trough caused the inflow of warmer and saltier water, and the entire thermohaline
631 structure of water below the sub-surface halocline has been uplifted (Figures 6c and 7). The
632 salinification also observed over the western flank of the glacier trough seems to be attributed to

633 both elevating of isohalines caused by upwelling and the off-shore residing of winter halostad. The
634 landfast ice extending during winter over the Wandel Sea shelfbreak and upper continental slope
635 damps upwelling, which starts to develop as soon as the outer portion of the landfast ice is
636 collapsed.

637

638 **4.2. Assessment of the seasonal cycle based on numerical simulations**

639 The preceding analysis motivated us to use an experiment of a high-resolution numerical model to
640 assess the PW flow along the Wandel sea upper continental slope and its seasonal variability. A
641 passive tracer was introduced into the model at Bering Strait from the beginning of the experiment
642 on January 1, 2002. A snapshot of the passive tracer fields in January 2010 shows that the model
643 reproduces two branches of the PW flow (i) following the Beaufort Sea continental slope and (ii)
644 crossing the Arctic Ocean to Fram Strait (Figure 12a) in agreement with a schematic circulation
645 of PW in Figure 1. In the western Fram Strait and Greenland Sea, the PW tracers are distributed
646 southward along the Greenland shelf and continental slope with concentration of PW up to 45 m
647 over the Wandel Sea shelfbreak. This tracer distribution is consistent with previous modelling by
648 *Hu and Myers* [2013] and *Aksenov et al.* [2016]. Further integration to December 2016 revealed
649 accumulation of PW in the Canada Basin and corresponding decrease of the PW outflow through
650 western Fram Strait (Figure 11b). This corroborates results by *Brugler et al.* [2014] showing that
651 that in recent years a significant portion of PW has been advected into the interior Canada Basin.
652 *Zhong et al.* [2018] suggested that the changing pathways of PW are related to the changing
653 position of the Beaufort Gyre and the intensification of geostrophic currents in the southwestern
654 Canada Basin. The PW accumulation in the Canada Basin from 2010 to 2016 results in a decrease
655 of the PW tracers over the Wandel Sea upper continental slope down to ~20 m (Figure 12b). By

656 July 2015 over the Wandel Sea outer shelf and upper continental slope, the PW tracers integrated
657 through the 20-85 m depth were reduced to 61 m and 47 m, respectively (Figures 12c and 12d).

658 The simulated seasonal cycle over the Wandel Sea outer shelf and upper continental slope
659 was explored using the 7-year mean seasonal anomalies generated for the two positions depicted
660 in Figure 10c. The seasonal anomalies were obtained by computing a representative year. For each
661 year, the mean was estimated, and then the anomalies for a given date were derived along with
662 standard deviations. Finally, they were averaged from 2010 to 2016 for the Wandel Sea continental
663 slope (Figure 13b) and outer shelf (Figure 13c). For both the outer shelf and continental slope the
664 PW variability is higher during winter and lower during summer. It is likely due to a more
665 persistent summer atmospheric forcing dominated by sustainable southerly winds (Figure 13a).
666 Over the upper continental slope the seasonality of the PW tracer's anomalies is very limited
667 (Figure 13b). In contrast, over the outer shelf the seasonal cycle is traceable, but not statistically
668 confident, partly due to significant variability of the PW anomalies during winter. Note that the
669 model does not take into account the landfast ice extension over the upper continental slope during
670 late winter, as we discuss below. The shelf-to-slope difference in seasonal cycling suggests that
671 the seasonal signal is generated locally rather than advected from the Canada Basin. Overall, the
672 numerical simulations reveal that (i) PW occupies the Wandel Sea outer shelf as also evident from
673 our mooring observations and (ii) the PW seasonal cycle is generated locally due to the seasonality
674 of wind over the Wandel Sea continental slope (Figure 13a) and associated Ekman transport of
675 PW. While the results of model simulations are not capable of fully reproducing the PW seasonal
676 cycle over the outer shelf, they are entirely consistent with conclusions obtained using
677 observational data on CTD, CDOM and currents.

678

679 **5. Summary and conclusions**

680 Over the Canada Basin, PW impacts the halocline structure, producing a double halocline with a
681 “cold Halostad” formed by the volumetric injection of the Pacific winter water. The ITP data from
682 the Wandel Sea shelf revealed that the sub-surface (~15-85 m depth) low stratified cold halostad
683 with salinities of 30-31.5, temperatures down to -1.7°C and high CDOM values resembles the
684 “cold Halostad” in the Canada Basin. Our results suggest that the Wandel Sea halostad is
685 maintained by the on-shelf inflow of PW modified en route to Fram Strait and advected along the
686 Wandel Sea shelfbreak and upper continental slope by the coastal branch of the PW outflow from
687 the Arctic Ocean.

688 Wind forcing over the northeast Greenland shows a northerly component during winter
689 favouring Ekman transport of the Pacific-derived Arctic water to the Wandel Sea outer shelf
690 (Figure 14a). As a result, a higher fraction of the Pacific-derived water significantly modifies the
691 outer shelf water column; the halostad is cooled, freshened and CDOM enriched, and its lower
692 boundary is deepened (Figures 14a and 14c). The northerly winds also favours the sea-ice Ekman
693 transport conditioning the landfast ice extension over the Wandel Sea shelfbreak and upper
694 continental slope (Figure 14a).

695 The prevailing southerly summer winds favour upwelling that results in retreat of the
696 Pacific-derived water off the shelf, but also forces the Atlantic water on-shelf inflow (Figure 14b).
697 The halostad lower boundary is shallowed, and halostad becomes saltier, warmer, and CDOM is
698 reduced, indicating the lower fraction of the Pacific-derived water on the shelf (Figures 14b and
699 14d). During winter the landfast ice extends over the upper continental slope and disrupts the wind-
700 driven seasonal patterns. The position of the landfast ice edge relative to the shelf slope break
701 illustrates the important role which landfast ice can play in coastal upwelling, consistent with

702 modelling of *Carmack and Chapman* [2003], and observations at other landfast ice edge locations
703 [e.g., *Tremblay et al.* 2011]). Once the landfast ice has collapsed, the upwelling favours the AW
704 on-shelf inflow accompanied by the PW outflow as indicated in Figure 14b.

705 The seasonal patterns of the Pacific-derived water over the Wandel Sea shelf are in
706 agreement with results of the CTD survey and numerical simulations. Simulations of the PW
707 tracers suggest a role of the local wind forcing for the PW on-shelf inflow during winter, but the
708 results on simulated seasonality are not statistically significant. It seems that the deficiencies of
709 the model simulations are conditioned by an incomplete definition of the landfast ice pointing out
710 a necessity for more realistic sea-ice parametrisation and higher spatial resolution over the Wandel
711 Sea continental slope area. Seasonality of the wind is the hypothesized cause of the halostad
712 variability, but probably does not provide a complete explanation. Several other mechanisms,
713 including dynamical instabilities and seasonal features of the East Greenland Current [e.g., *Bacon*
714 *et al.*, 2002] may contribute to the lateral displacement of the PW flow relative to the Wandel Sea
715 shelfbreak and upper continental slope. Future research in this hard to access region will help
716 clarify our findings.

717

718 **Acknowledgements:** This study was funded by the Canada Excellence Research Chair program
719 (SR), the Canada Research Chair program (DB), the Canada Foundation of Innovation, the
720 National Sciences and Engineering Research Council of Canada – NSERC (grant RGPIN-2014-
721 03606, ID), the Manitoba Research and Innovation Fund, the University of Manitoba, Aarhus
722 University, the Greenland Institute of Natural Resources, and the EU project NACLIM (grant
723 agreement 308299, BR). PGM was supported by the NSERC grants RGPIN 227438-09, RGPIN
724 04357, and RGPCC 433898. The model experiment was performed on Compute Canada

725 infrastructure. The NEMO model is available through the NEMO website [http://www.nemo-](http://www.nemo-ocean.eu/)
 726 [ocean.eu/](http://www.nemo-ocean.eu/). The ANHA configuration and its output can be accessed at
 727 <http://knossos.eas.ualberta.ca/xianmin/anha/index.html>. We thank Ivali Lennert, Kunuk Lennert
 728 and Egon Frandsen for technical assistance in the field. We also appreciate outstanding logistical
 729 support from the Station Nord Danish military personnel. This work is a contribution to the Arctic
 730 Science Partnership (ASP) and the ArcticNet Networks of Centres of Excellence programs. The
 731 mooring oceanographic data are available through the Polar Data Catalogue at
 732 <https://www.polardata.ca>.

733

734 6. Reference

735 Alkire, M. B., K. K. Falkner, T. Boyd, and R. W. Macdonald (2010), Sea-ice melt and meteoric
 736 water distributions in Baffin Bay and the Canadian Arctic archipelago, *J. Mar. Res.*, 68(6), 767-
 737 798, doi: 10.1357/002224010796673867.

738 Aksenov, Y., et al. (2016), Arctic pathways of Pacific Water: Arctic Ocean Model Intercomparison
 739 experiments, *J. Geophys. Res. Oceans*, 121, 27–59, doi:10.1002/2015JC011299.

740 Amon, R. M. W., G. Bude'us, and B. Meon (2003), Dissolved organic carbon distribution and
 741 origin in the Nordic Seas: Exchanges with the Arctic Ocean and the North Atlantic, *J. Geophys.*
 742 *Res.*, 108(C7), 3221, doi:10.1029/2002JC001594.

743 Bacon, S., G. Reverdin, I. G. Rigor, and H. M. Smith (2002), A freshwater jet on the east Greenland
 744 shelf, *J. Geophys. Res.*, 107(C7), 3068, doi:10.1029/2001JC000935.

745 Bamber, J. L., R. M. Westaway, B. Marzeion, and B. Wouters (2018), The land ice contribution
 746 to sea level during the satellite era, *Environ. Res. Lett.*, 13, 063008, doi:10.1088/1748-
 747 9326/aac2f0.

748 Bendtsen, J., J. Mortensen, K. Lennert, J. K. Ehn, W. Boone, V. Galindo, Y. Hu, I. A. Dmitrenko,
 749 S. A. Kirillov, K. K. Kjeldsen, Y. Kristoffersen, D. G. Barber, and S. Rysgaard (2017), Sea ice
 750 breakup and marine melt of a retreating tidewater outlet glacier in northeast Greenland (81 N),
 751 *Scientific Reports*, 7(1), 4941, doi:10.1038/s41598-017-05089-3.

752 Bignami, F. and T. S. Hopkins (1997), The water mass characteristics of the Northeast Water
 753 Polynya: Polar Sea data 1992–1993, *J. Marine Sys.*, 10, 139-156.

754 Budéus, G., W. Schneider and G. Kattner (1997), Distribution and exchange of water masses in
 755 the Northeast Water polynya (Greenland Sea), *J. Marine Sys.*, 10, 139-156.

- 756 Brugler, E. T., R. S. Pickart, G. W. K Moore, S. Roberts, T. J. Weingartner, and H. Statscewich
757 (2014), Seasonal to interannual variability of the Pacific water boundary current in the Beaufort
758 Sea, *Progress in Oceanography*, 127, 1–20, doi: 10.1016/j.pocean.2014.05.002.
- 759 Carmack, E. C., et al. (2016), Freshwater and its role in the Arctic Marine System: Sources,
760 disposition, storage, export, and physical and biogeochemical consequences in the Arctic and
761 global oceans, *J. Geophys. Res. Biogeosci.*, 121, 675–717, doi:10.1002/2015JG003140.
- 762 Courtois, P., X. Hu, C. Pennelly, P. Spence, and P. G. Myers (2017), Mixed layer depth calculation
763 in deep convection regions in ocean numerical models, *Ocean Modelling*, 120, 60-78, doi:
764 10.1016/j.ocemod.2017.10.007.
- 765 Castro de la Guardia L., X. Hu, and P. G. Myers (2015), Potential positive feedback between
766 Greenland Ice Sheet melt and Baffin Bay heat content on the west Greenland shelf, *Geophys. Res.*
767 *Let.*, 42(12), 4922-4930, doi: 10.1002/2015GL064626.
- 768 de Steur, L., M. Steele, E. Hansen, J. Morison, I. Polyakov, S. M. Olsen, H. Melling, F. A.
769 McLaughlin, R. Kwok, W. M. Smethie Jr., and P. Schlosser (2013), Hydrographic changes in the
770 Lincoln Sea in the Arctic Ocean with focus on an upper ocean freshwater anomaly between 2007
771 and 2010, *J. Geophys. Res. Oceans*, 118, 4699–4715, doi:10.1002/jgrc.20341.
- 772 Dmitrenko, I., I. Polyakov, S. Kirillov, L. Timokhov, H. Simmons, V. Ivanov, and D. Walsh
773 (2006), Seasonal Variability of Atlantic Water on the Continental Slope of the Laptev Sea during
774 2002-2004, *Earth and Planetary Science Let.*, 244(3-4), 735-743, doi:
775 10.1016/j.epsl.2006.01.067.
- 776 Dmitrenko, I. A., S. A. Kirillov, V. V. Ivanov, R. A. Woodgate, I. V. Polyakov, N. Koldunov, L.
777 Fortier, C. Lalande, L. Kaleschke, D. Bauch, J. A. Hölemann, and L. A. Timokhov (2009),
778 Seasonal modification of the Arctic Ocean intermediate water layer off the eastern Laptev Sea
779 continental shelf break, *J. Geophys. Res.*, 114, C06010, doi:10.1029/2008JC005229.
- 780 Dmitrenko, I. A., S. A Kirillov, S. Rysgaard, D. G. Barber, D. G. Babb, L. T. Pedersen, N. V.
781 Koldunov, W. Boone, O. Crabeck and J. Mortensen (2015), Polynya impacts on water properties
782 in a Northeast Greenland fjord, *Estuarine, Coastal and Shelf Sci.*, 153, 10-17, doi:
783 10.1016/j.ecss.2014.11.027.
- 784 Dmitrenko, I. A., S. A. Kirillov, B. Rudels, D. G. Babb, L. T. Pedersen, S. Rysgaard, Y.
785 Kristoffersen, and D. G. Barber (2017), Arctic Ocean outflow and glacier-ocean interaction modify
786 water over the Wandel Sea shelf, northeast Greenland, *Ocean Sci.*, 13, 1045–1060, doi:
787 10.5194/os-13-1045-2017.
- 788 Dodd, P. A., K. J. Heywood, M. P. Meredith, A. C. Naveira-Garabato, A. D. Marca, and K. K.
789 Falkner (2009), Sources and fate of freshwater exported in the East Greenland Current, *Geophys.*
790 *Res. Let.*, 36, L19608, doi:10.1029/2009GL039663.
- 791 Dodd, P. A., B. Rabe, E. Hansen, E. Falck, A. Mackensen, E. Rohling, C. Stedmon, and S.
792 Kristiansen (2012), The freshwater composition of the Fram Strait outflow derived from a decade
793 of tracer measurements, *J. Geophys. Res.*, 117, C11005, doi:10.1029/2012JC008011.

- 794 Falck, E. (2001), Contribution of waters of Atlantic and Pacific origin in the Northeast Water
795 Polynya, *Polar Res.*, 20(2), 193–200, doi:10.1111/j.1751-8369.2001.tb00056.x.
- 796 Falck, E., G. Kattner, and G. Bude'us (2005), Disappearance of Pacific Water in the northwestern
797 Fram Strait, *Geophys. Res. Lett.*, 32, L14619, doi:10.1029/2005GL023400.
- 798 Fichefet, T. and M. A. M. Maqueda (1997), Sensitivity of a global sea ice model to the treatment
799 of ice thermodynamics and dynamics, *J. Geophys. Res.*, 102, 12 609–12 646,
800 doi:10.1029/97JC00480.
- 801 Granskog, M. A., C. A. Stedmon, P. A. Dodd, R. M. W. Amon, A. K. Pavlov, L. de Steur, and E.
802 Hansen (2012), Characteristics of colored dissolved organic matter (CDOM) in the Arctic outflow
803 in the Fram Strait: Assessing the changes and fate of terrigenous CDOM in the Arctic Ocean, *J.*
804 *Geophys. Res.*, 117, C12021, doi:10.1029/2012JC008075.
- 805 Guardia, de la L. C., X. Hu, and P. G. Myers (2015), Potential positive feedback between
806 Greenland Ice Sheet melt and Baffin Bay heat content on the west Greenland shelf, *Geophys. Res.*
807 *Lett.*, 42, 4922–4930, doi:10.1002/2015GL064626.
- 808 Guéguen, C., L. Guo, M. Yamamoto-Kawai, and N. Tanaka (2007), Colored dissolved organic
809 matter dynamics across the shelf-basin interface in the western Arctic Ocean, *J. Geophys. Res.*,
810 112, C05038, doi:10.1029/2006JC003584.
- 811 Guay, C. K., G. P. Klinkhammer, K. K. Falkner, R. Benner, P. G. Coble, T. E. Whitledge, B.
812 Black, J. F. Bussell, and T. A. Wagner (1999), High-resolution measurements of dissolved organic
813 carbon in the Arctic Ocean by in situ fiber-optic spectrometry, *Geophys. Res. Lett.*, 26(8), 1007–
814 1010, doi:10.1029/1999GL900130.
- 815 Haine, T. W. N., B. Curry, R. Gerdes, E. Hansen, M. Karcher, C. Lee, B. Rudels, G. Spreen, L. de
816 Steur, K. D. Stewart, and R. Woodgate (2015), Arctic freshwater export: Status, mechanisms, and
817 prospects, *Global and Planetary Change*, 125, 13–35, doi:10.1016/j.gloplacha.2014.11.013.
- 818 Holland, M. M., J. Finnis, A. P. Barrett, and M. C. Serreze (2007), Projected changes in Arctic
819 Ocean freshwater budgets, *J. Geophys. Res.*, 112, G04S55, doi:10.1029/2006JG000354.
- 820 Hu, X. and P. G. Myers (2013), A Lagrangian view of Pacific water inflow pathways in the Arctic
821 Ocean during model spin-up, *Ocean Modelling*, 71, 66–80, doi:10.1016/j.ocemod.2013.06.007.
- 822 Hu, X., J. Sun, T. O. Chan, and P. G. Myers (2018), Thermodynamic and Dynamic Ice Thickness
823 Changes in the Canadian Arctic Archipelago in NEMO-LIM2 Numerical Simulations,
824 *Cryosphere*, 12, 1233-1247, doi:10.5194/tc-12-1233-2018.
- 825 Hunke, E. C. and J. K. Dukowicz, (1997), An elastic-viscous-plastic model for sea ice dynamics,
826 *Journal of Physical Oceanography*, 27, 1849–1867, doi:10.1175/1520-
827 0485(1997)027<1849:AEVPMF>2.0.CO;2.
- 828 Jones, E. P., J. H. Swift, L. G. Anderson, M. Lipizer, G. Civitarese, K. K. Falkner, G. Kattner, and
829 F. McLaughlin (2003), Tracing Pacific water in the North Atlantic Ocean, *J. Geophys. Res.*,
830 108(C4), 3116, doi:10.1029/2001JC001141, 2003.

- 831 Kalnay, E., et al. (1996), The NCEP/NCAR 40-Year Reanalysis Project, *Bull. Amer. Meteor. Soc.*,
832 77, 437–471, doi:10.1175/1520-0477(1996)077<0437:TNYRP>2.0.CO;2.
- 833 Kirillov, S., I. Dmitrenko, S. Rysgaard, D. Babb, L. Toudal Pedersen, J. Ehn, J. Bendtsen, and D.
834 Barber (2017), Storm-induced water dynamics and thermohaline structure at the tidewater Flade
835 Isblink Glacier outlet to the Wandel Sea (NE Greenland), *Ocean Sci.*, 13, 947-959, doi:
836 10.5194/os-13-947-2017.
- 837 Kirillov S., I. Dmitrenko, S. Rysgaard, D. Babb, J. Ehn, J. Bendtsen, W. Boone, D. Barber, and
838 N.-X. Geilfus (2018), The inferred formation of a sub-ice platelet layer below the multiyear
839 landfast sea ice in the Wandel Sea (NE Greenland) induced by meltwater drainage, *J. Geophys.*
840 *Res. Oceans*, doi:10.1029/2017JC013672.
- 841 Limoges, A., S. Ribeiro, K. Weckström, M. Heikkilä, K. Zamelczyk, T. J. Andersen, P. Tallberg,
842 G. Massé, S. Rysgaard, N. Nørgaard-Pedersen, and M.-S. Seidenkrantz (2018), Linking the
843 modern distribution of biogenic proxies in High Arctic Greenland shelf sediments to sea ice,
844 primary production, and Arctic-Atlantic inflow, *J. Geophys. Res.: Biogeosciences*, 123, 760-786,
845 doi: 10.1002/2017JG003840.
- 846 Madec, G. and the NEMO team: NEMO ocean engine (2008), Note du Pôle de modélisation,
847 Institut Pierre-Simon Laplace (IPSL), France, 27, ISSN No 1288-1619.
- 848 Masina, S., A. Storto, N. Ferry, M. Valdivieso, K. Haines, M. Balmaseda, H. Zuo, M. Drevillon,
849 and L. Parent (2017), An ensemble of eddypermitting global ocean reanalyses from the MyOcean
850 project, *Climate Dynamics*, 49, 813-841, doi: 10.1007/s00382-015-2728-5.
- 851 McLaughlin, F. A., E. C. Carmack, R. W. MacDonald, H. Melling, J. H. Swift, P. A. Wheeler, B.
852 F. Sherr and E. B. Sherr (2004), The joint roles of Pacific and Atlantic-origin waters in the Canada
853 Basin, 1997–1998, *Deep Sea Res. Part I*, 51, 107–128.
- 854 Morison, J, R. Kwok, C. Peralta-Ferriz, M. Alkire, I. Rigor, R. Andersen, and M. Steele (2012),
855 Changing Arctic Ocean freshwater pathways, *Nature*, 481(7379), 66-70, doi:
856 10.1038/nature10705.
- 857 Nørgaard-Pedersen, N, S. Ribeiro, N. Mikkelsen, A. Limoges and M. S. Seidenkrantz (2016),
858 Investigations of past climate and sea-ice variability in the fjord area by Station Nord, eastern
859 North Greenland, *Geological Survey of Denmark and Greenland Bulletin*, 35, 67-70.
- 860 Palmer, S. J., A. Shepherd, A. Sundal, E. Rinne, and P. Nienow (2010), InSAR observations of ice
861 elevation and velocity fluctuations at the Flade Isblink ice cap, eastern North Greenland, *J.*
862 *Geophys. Res.*, 115, F04037, doi:10.1029/2010JF001686.
- 863 Prowse, T., A. Bring, J. Mård, and E. Carmack (2015), Arctic Freshwater Synthesis: Introduction,
864 *J. Geophys. Res. Biogeosci.*, 120, 2121–2131, doi:10.1002/2015JG003127.
- 865 Rabe, B., M. Karcher, U. Schauer, J. M. Toole, R. A. Krishfield, S. Pisarev, F. Kauker, R. Gerdes,
866 and T. Kikuchi (2011), An assessment of Arctic Ocean freshwater content changes from the 1990s
867 to the 2006–2008 period, *Deep Sea Res., Part I*, 58(2), 173–185, doi:10.1016/j.dsr.2010.12.002.

- 868 Rinne, E. J., A. Shepherd, S. Palmer, M. R. van den Broeke, A. Muir, J. Ettema, and D. Wingham
869 (2011), On the recent elevation changes at the Flade Isblink Ice Cap, northern Greenland, *J.*
870 *Geophys. Res.*, 116, F03024, doi:10.1029/2011JF001972.
- 871 Rodell, M., S. Famiglietti, D. N. Wiese, J. T. Reager, H. K. Beaulieu, F. W. Landerer, and M.-
872 H. Lo (2018), Emerging trends in global freshwater availability, *Nature*,
873 <https://doi.org/10.1038/s41586-018-0123-1>.
- 874 Serreze, M. C., A. P. Barrett, A. G. Slater, R. A. Woodgate, K. Aagaard, R. B. Lammers, M. Steele,
875 R. Moritz, M. Meredith, and C. M. Lee (2006), The large-scale freshwater cycle of the Arctic, *J.*
876 *Geophys. Res.*, 111, C11010, doi:10.1029/2005JC003424.
- 877 Shimada, K., M. Itoh, S. Nishino, F. McLaughlin, E. Carmack, and A. Proshutinsky (2005),
878 Halocline structure in the Canada Basin of the Arctic Ocean, *Geophys. Res. Lett.*, 32, L03605,
879 doi:10.1029/2004GL021358.
- 880 Shroyer, E. L., and R. S. Pickart (2018), Pathways, timing, and evolution of Pacific Winter Water
881 through Barrow Canyon, *Deep Sea Res.*, Part II, in press, doi: 10.1016/j.dsr2.2018.05.004.
- 882 Smith, G. C., F. Roy, P. Mann, F. Dupont, B. Brasnett, J.-F. Lemieux, S. Laroche, and S. Bélair
883 (2014), A new atmospheric dataset for forcing ice–ocean models: Evaluation of reforecasts using
884 the Canadian global deterministic prediction system, *Q. J. R. Meteorol. Soc.*, 140, 881–894,
885 DOI:10.1002/qj.2194.
- 886 Stedmon, C. A., M. A. Granskog, and P. A. Dodd (2015), An approach to estimate the freshwater
887 contribution from glacial melt and precipitation in East Greenland shelf waters using colored
888 dissolved organic matter (CDOM), *J. Geophys. Res. Oceans*, 120, 1107–1117,
889 doi:10.1002/2014JC010501.
- 890 Stedmon, C. A., R. M. W. Amon, A. J. Rinehart, and S. A. Walker (2009), The supply and
891 characteristics of colored dissolved organic matter (CDOM) in the Arctic Ocean: Pan Arctic trends
892 and differences, *Marine Chemistry*, 124(1–4), 108–118, doi: 10.1016/j.marchem.2010.12.007.
- 893 Steele, M., J. Morison, W. Ermold, I. Rigor, M. Ortmeyer, and K. Shimada (2004), Circulation of
894 summer Pacific halocline water in the Arctic Ocean, *J. Geophys. Res.*, 109, C02027,
895 doi:10.1029/2003JC002009.
- 896 Sutherland, D. A., and R. S. Pickart (2008), The East Greenland Coastal Current: Structure,
897 variability, and forcing, *Prog. Oceanogr.*, 78(1), 58–77, doi:10.1016/j.pcean.2007.09.006.
- 898 Sutherland, D. A., R. S. Pickart, E. Peter Jones, K. Azetsu-Scott, A. Jane Eert, and J. Ólafsson
899 (2009), Freshwater composition of the waters off southeast Greenland and their link to the Arctic
900 Ocean, *J. Geophys. Res.*, 114, C05020, doi:10.1029/2008JC004808.
- 901 Tremblay, J. E., S. Bélanger, D. G. Barber, M. Asplin, J. Martin, G. Darnis, L. Fortier, Y. Gratton, H. Link,
902 P. Archambault, A. Sallon, C. Michel, W. G. Williams, B. Philippe, and M. Gosselin (2011), Climate
903 forcing multiplies biological productivity in the coastal Arctic Ocean, *Geophys. Res. Lett.*, 38,
904 doi:10.1029/2011GL048825.

905 Timmermans, M.-L., J. Marshall, A. Proshutinsky, and J. Scott (2017), Seasonally derived
 906 components of the Canada Basin halocline, *Geophys. Res. Lett.*, 44, 5008–5015,
 907 doi:10.1002/2017GL073042.

908 Timmermans, M.-L., A. Proshutinsky, E. Golubeva, J. M. Jackson, R. Krishfield, M. McCall, G.
 909 Platov, J. Toole, W. Williams, T. Kikuchi, and S. Nishino (2014), Mechanisms of Pacific Summer
 910 Water variability in the Arctic's Central Canada Basin, *J. Geophys. Res. Oceans*, 119, 7523–7548,
 911 doi:10.1002/2014JC010273.

912 Watanabe, J. (2013), Linkages among halocline variability, shelf-basin interaction, and wind
 913 regimes in the Beaufort Sea demonstrated in pan-Arctic Ocean modeling framework, *Ocean*
 914 *Modelling*, 71, 43–53, doi:10.1016/j.ocemod.2012.12.010.

915 Woodgate, R. A., K. Aagaard, and T. J. Weingartner (2005), Monthly temperature, salinity, and
 916 transport variability of the Bering Strait through flow, *Geophys. Res. Lett.*, 32, L04601,
 917 doi:10.1029/2004GL021880.

918 Woodgate, R. A., T. J. Weingartner, and R. Lindsay (2012), Observed increases in Bering Strait
 919 oceanic fluxes from the Pacific to the Arctic from 2001 to 2011 and their impacts on the Arctic
 920 Ocean water column, *Geophys. Res. Lett.*, 39, L24603, doi:10.1029/2012GL054092.

921 Woodgate, R. (2013), Arctic Ocean Circulation: Going Around At the Top Of the World, *Nature*
 922 *Education Knowledge*, 4(8), 8.

923

924

925 **Figure captions**

926 **Figure 1:** Schematic circulation of the Pacific Water (PW, red arrows) in the Arctic Ocean and
 927 adjoining Greenland Sea following *Jones* [2001] and *Woodgate* [2013]. The pink arrow indicates
 928 the East Greenland Current. The red dot depicts the position of Station Nord in northeast
 929 Greenland.

930 **Figure 2:** (a) Station Nord (SN) on the Greenland map. The pink shading highlights the Wandel
 931 Sea region with the adjoining fjord system and Northeast Water Polynya (NEW) area enlarged in
 932 (b). (b) The MODIS/TERRA satellite image from 22 August 2014 taken over the SN/NEW area.
 933 Red circled cross indicates the mooring. Red cross depicts SN. The dashed blue rectangle indicates

934 the 2015 study area shown in Figure 3. Gray arrows schematically depict the coastal branch of the
935 Pacific-derived Arctic water flow suggested by *Dmitrenko et al.* [2017].

936 **Figure 3:** (a) The Sentinel-1 C-band SAR image from 2 February 2015 with the CTD stations and
937 mooring overlaid. Colored circles identify CTD stations used for this research with CTDs showing
938 winter (blue), summer (red) and transitional (green) modes of the Pacific-derived halostad as
939 depicted with similar colors in Figure 5. Depth shown by white contour lines. Blue arrows indicate
940 the northern outlet glaciers of the Flade Isblink ice cap. The lighter areas indicate the multi-year
941 landfast ice (~2 m to > 4 m thick). (b) Aerial photo taken from the aircraft before landing at Station
942 Nord on May 2017 shows icebergs grounded on the marginal lateral moraine flanking the
943 southwestern rim of the glacier trough; credits: I. Dmitrenko.

944 **Figure 4:** The Sentinel-1 C-band SAR images from (a) 19 August 2015 and (b) 4 April 2016 with
945 the CTD stations and mooring overlaid. Colored circles identify CTD stations used for this
946 research with CTDs showing winter (blue), summer (red) and glacier (purple) modes of the
947 Pacific-derived halostad as depicted with similar colors in Figure 5. (a) The dark areas indicate the
948 open water. (c) Aerial photo taken over the tidewater glacier outlet in May 2017; purple arrow
949 highlights the glacier bay where CTDs occupied in April 2016 (credits: I. Dmitrenko). The spatial
950 scale at left bottom is approximate.

951 **Figure 5:** Vertical distribution of (a, d and f) temperature (°C) and (b, c, e and g) salinity over the
952 southeastern Wandel Sea shelf (>60 m depth) in (a,b,c) April-May 2015, (d,e) 20-21 August 2015
953 and (f,g) 4-8 April 2016 through the upper 100-m layer. Red, blue, green and purple lines indicate
954 the summer, winter, transitional and glacier modes, respectively. Dashed lines show moored ITP
955 profiles. Dotted lines in a and b are from station #65 (see Figure 3). Gray dashed lines in d-g are

956 the ITP profiles taken in 15 May 2015 as in **a-c**. Blue and pink shading highlights the Pacific-
957 derived halostad and Atlantic-derived halocline, respectively.

958 **Figure 6:** Progressive vector diagram for the ADCP 2-m binned current record at **(a)** 8 m, **(b)** 50
959 m and **(c)** 160 m depth. Blue and green lines highlight on-shelf inflow **(b)** across the shelfbreak
960 and **(c)** along the submarine glacier valley, respectively. **(a, b)** Red line highlights shelf outflow.
961 Purple lines indicate storm events also depicted in Figures 7 and 9. Dashed line indicates no
962 reliable data. Numbers show the Julian days.

963 **Figure 7:** **(a)** Schematic depictions show the on-shelf inflow (blue and green shading and arrows)
964 and outflow (pink shading and red arrows) events based on ADCP data for (top) 8 m, (middle) 50
965 m and (bottom) 160 m depth. **(b)** Temperature ($^{\circ}\text{C}$), **(c)** salinity, and **(d)** CDOM fluorescence
966 (ex/em 370/460 nm, ppb) from the Ice Tethered Profiler (ITP) deployed over the southeastern
967 Wandel Sea shelf from 15 May 2015 to 6 April 2016. Red-dashed rectangular indicates storm
968 events associated with southerly and southwesterly winds over the Wandel Sea continental slope
969 with their reference numbers from I to IV at the bottom. Color shading at the bottom highlights
970 different periods of CTD and CDOM variability.

971 **Figure 8:** In situ TS scatterplots of the temperature, salinity and CDOM time series from the
972 mooring during **(a)** stable, **(b)** transitional, **(c)** relaxation, and **(d)** stable periods. CDOM
973 fluorescence (ppb) is shown in color. The gray dashed lines are potential isopycnals in kg m^{-3} . The
974 dashed blue line is surface freezing temperature. Black-dotted lines indicate the bounds defining
975 the different water masses in the western Beaufort Sea following *von Appen and Pickart* [2012]:
976 the 33 line separates the Pacific ($31 < S < 33$) from the Atlantic ($S > 33$) water, and the -1°C line
977 separates the Pacific summer and winter water. Red line shows in situ mean TS diagram for the
978 cross-slope eastern Beaufort Sea section adopted from *Dmitrenko et al.* [2016].

979 **Figure 9:** Time series of the NCEP-derived 24-h mean 10-m **(a)** zonal and **(b)** meridional wind
980 (m s^{-1}) over the Wandel Sea continental slope at 82°N , 15°W (position depicted by white circles
981 in **c-d**) from April 2015 to April 2016. Purple line shows the 30-day running mean. Blue and green
982 shading and arrows highlight the on-shelf inflow at 50 m and 160 m depth, respectively. Pink
983 shading and red arrows highlight shelf outflow at 50 m depth. Red-dashed rectangular indicates
984 storm events associated with southerly and southwesterly winds over the Wandel Sea continental
985 slope with their reference numbers at the top. Color shading at the bottom highlights different
986 periods of CTD and CDOM variability as of Figure 7. Red arrow at the bottom identifies the day
987 when the landfast ice was collapsed over the Wandel Sea continental slope. The MODIS/TERRA
988 satellite images show the evolution of the landfast ice from **(c)** 30 June to **(d)** 30 July 2015. Red
989 circle and cross depict mooring and SN, respectively.

990 **Figure 10:** The Sentinel-1 C-band SAR images taken over the Wandel Sea and NEW at the
991 beginning of storm events # **(a)** I and **(c)** II and 24-h following the meridional wind maxima over
992 the Wandel Sea continental slope for storm events # **(b)** I, **(d)** II, **(e)** III and **(f)** IV. Red arrows
993 indicate the 24-h mean direction and velocity of maximal wind according to scale shown in **f**. Red
994 circle and cross depict mooring and SN, respectively. **(c)** Blue crosses indicate positions over the
995 Wandel Sea outer shelf and continental slope where the time series of the PW tracers shown in
996 Figures 12c and 12d, respectively.

997 **Figure 11:** Color shading shows daily mean **(a, e)** temperature ($^\circ\text{C}$), **(b, f)** salinity and **(c, g)**
998 CDOM (ppb) anomalies at 50 m depth from the moored ITP versus NCEP daily mean 10-m wind
999 over the Wandel Sea continental slope (top) and daily mean currents at 50 m depth (bottom) from
1000 15 May to 26 December 2015. Scatter plots show daily mean **(d)** winds and **(h)** currents used for
1001 computing **a-c** and **e-g**, respectively. Black dashed line depicts the along-slope direction derived
1002 from the International Bathymetric Chart of the Arctic Ocean (IBCAO).

1003 **Figure 12:** Simulated PW tracers concentration (m) for (a) 1-5 January 2010 and (b) 27-31
1004 December 2016 and time series of the PW tracers integrated through the 20-85 m depth layer over
1005 the Wandel Sea (c) continental slope at 82°20'N, 17°40'W and (d) outer shelf at 82°10'N, 18°40'W,
1006 as depicted in Figure 8c. (c, d) Pink shading highlights period of mooring record.

1007 **Figure 13:** (a) NCEP-derived 7-year mean (2010-2016) 10-m meridional wind (pink, m s^{-1}) over
1008 the Wandel Sea continental slope with its standard deviation on the top (blue). Blue and red thick
1009 lines show the 30-day running mean. The 7-year mean (2010-2016) anomalies of the simulated
1010 PW tracers concentration anomalies (m) integrated through the 20-85 m depth layer over the
1011 Wandel Sea (b) continental slope and (c) outer shelf. Gray shading highlights \pm one standard
1012 deviation. Pink shading highlights period dominated by southerly winds. Red and blue dashed lines
1013 show mean for periods dominated by southerly and northerly winds, respectively.

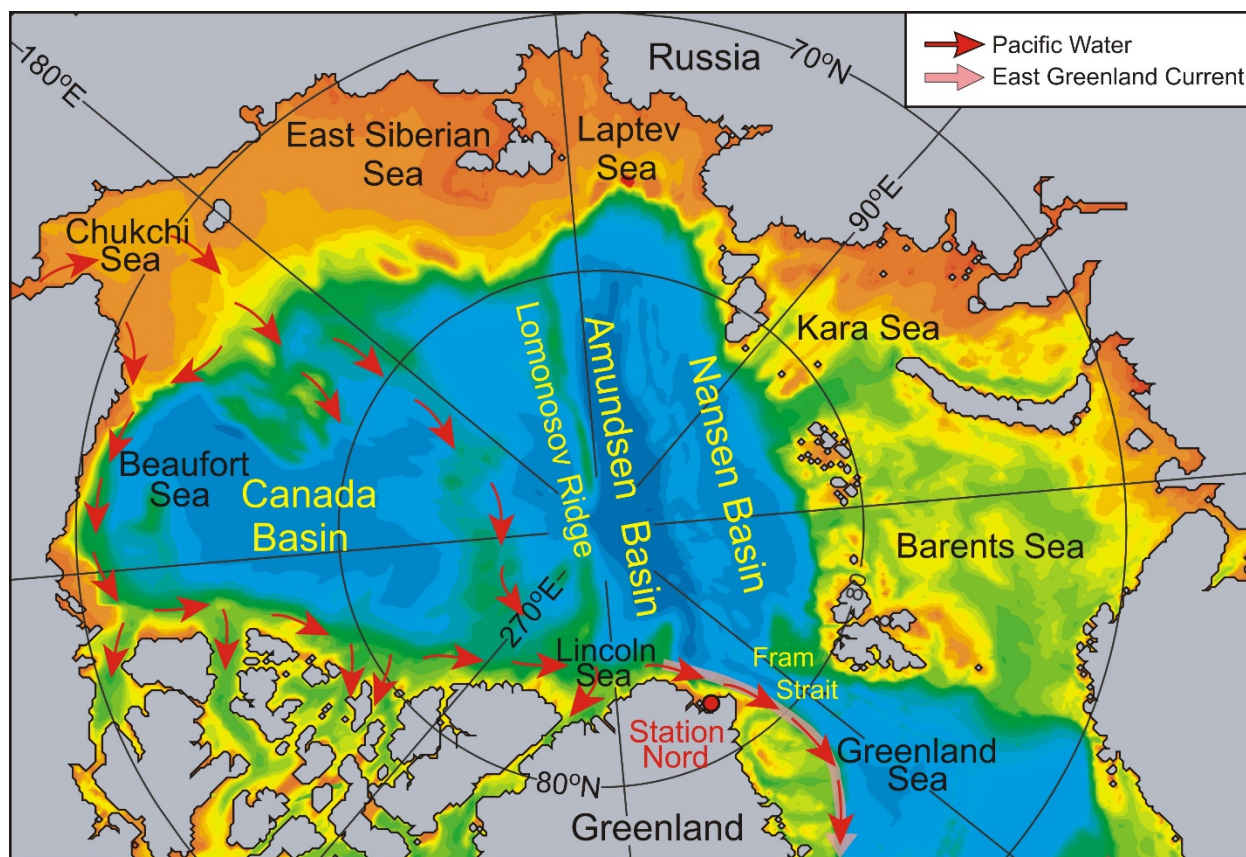
1014 **Figure 14:** Schematic depictions suggest lateral displacement of the Pacific-derived halostad in
1015 response to (a) 'winter' (November-April) northerly and (b) 'summer' (May-October) southerly
1016 wind forcing over the Wandel Sea continental slope with corresponding ITP CTD and CDOM
1017 vertical profiles shown in (c) and (d), respectively. (d) Dotted lines show summer profiles for
1018 comparison. Winter (cooler, fresher and CDOM enriched) and summer (warmer, saltier and less
1019 CDOM) modes of Pacific-derived halostad are identified as (a, c) wPW and (b, d) sPW,
1020 respectively.

1021 **Figures**

1022

1023

1024

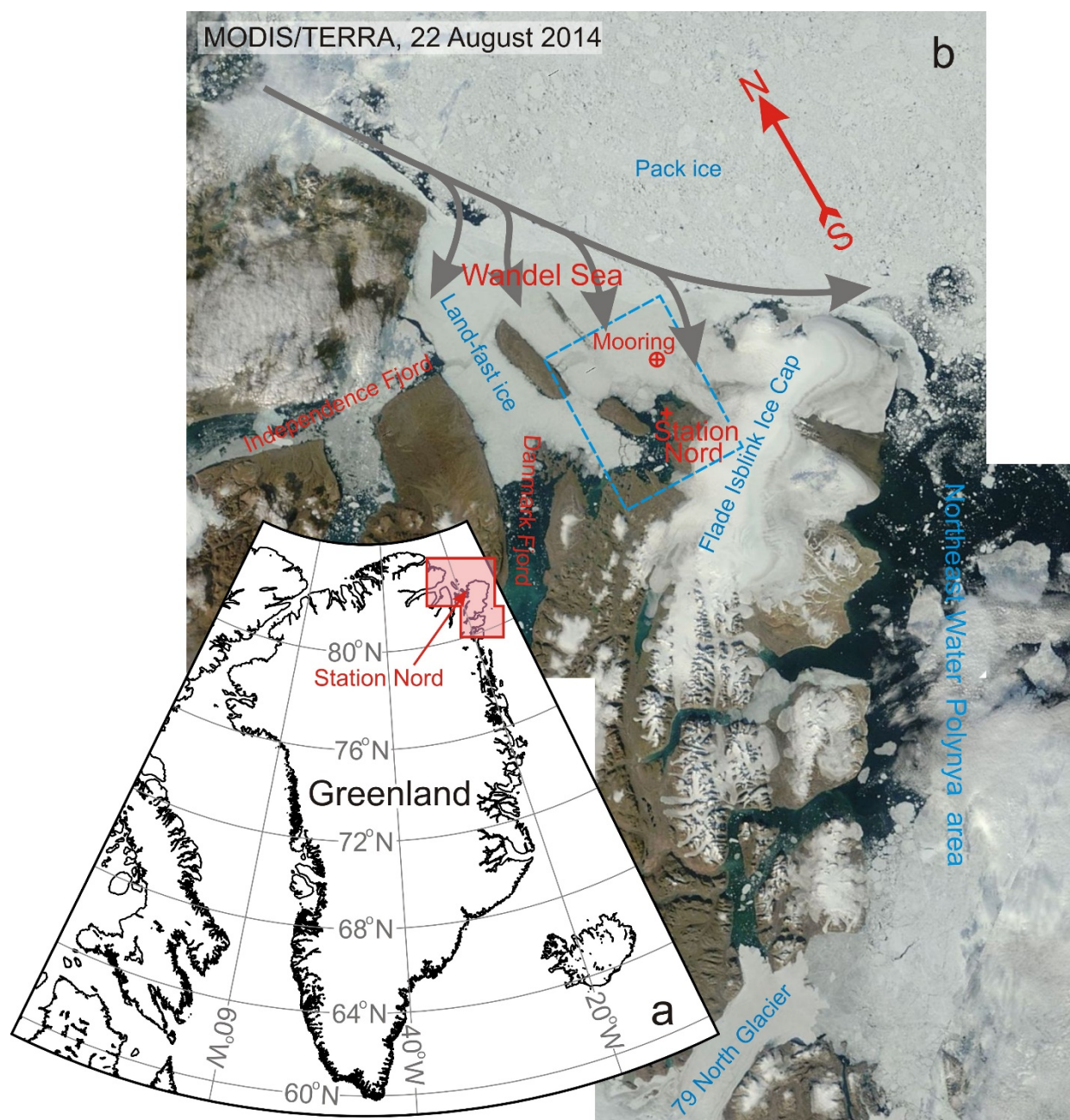


1025

1026 **Figure 1:** Schematic circulation of the Pacific Water (PW, red arrows) in the Arctic Ocean and
 1027 adjoining Greenland Sea following *Jones [2001]* and *Woodgate [2013]*. The pink arrow indicates
 1028 the East Greenland Current. The red dot depicts the position of Station Nord in northeast
 1029 Greenland.

1030

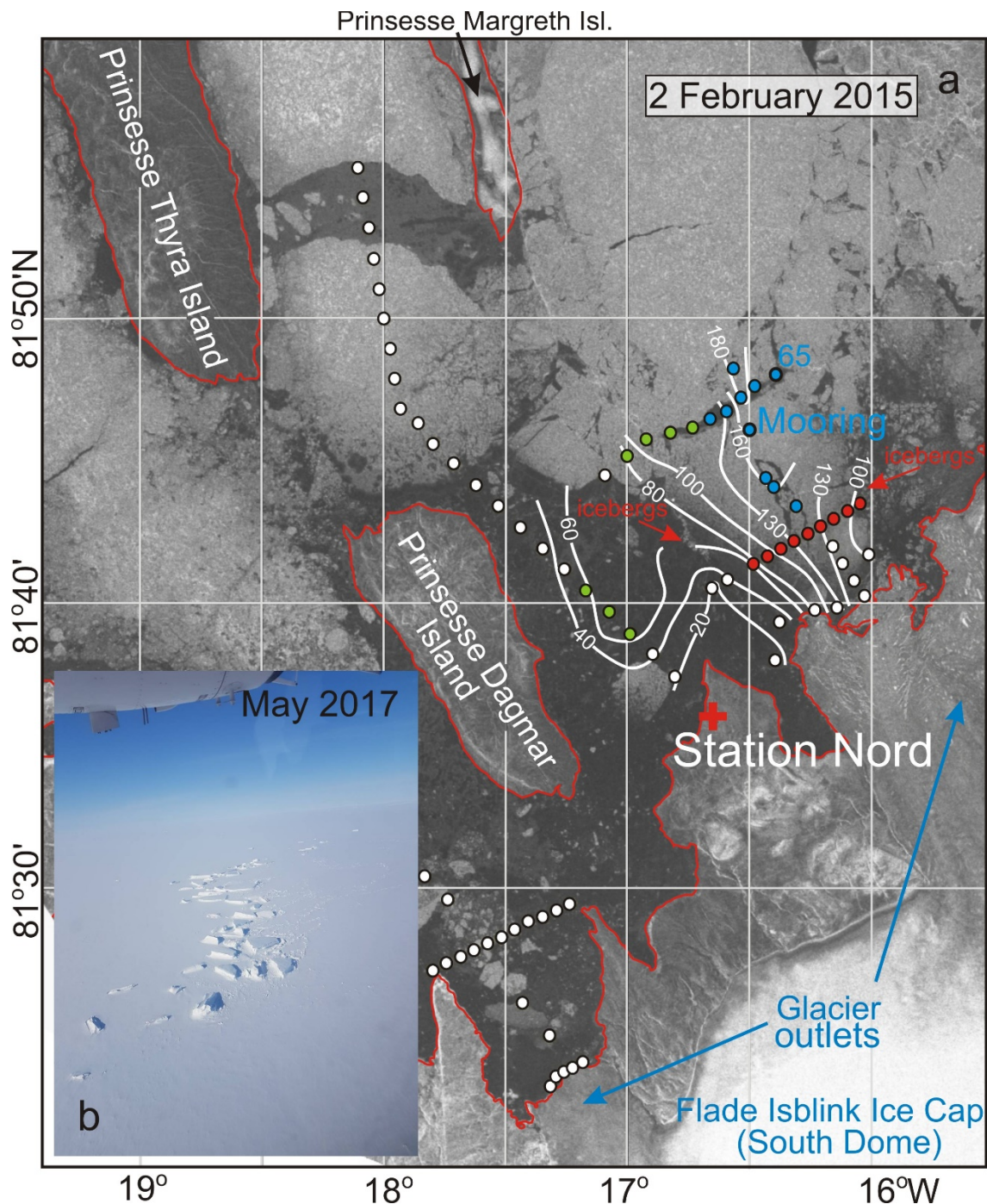
1031



1032

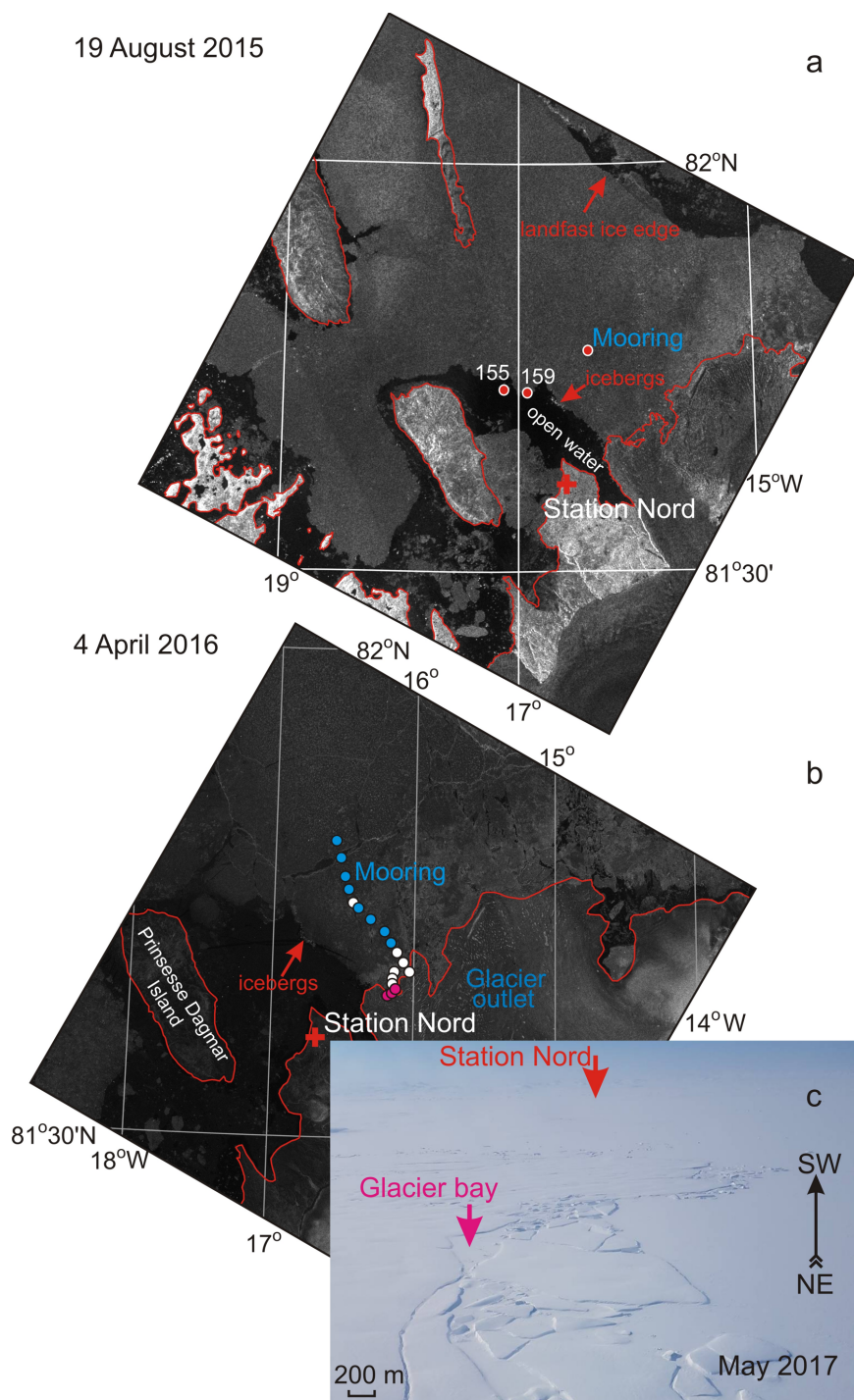
1033 **Figure 2:** (a) Station Nord (SN) on the Greenland map. The pink shading highlights the Wandel
 1034 Sea region with the adjoining fjord system and Northeast Water Polynya (NEW) area enlarged in
 1035 (b). (b) The MODIS/TERRA satellite image from 22 August 2014 taken over the SN/NEW area.
 1036 Red circled cross indicates the mooring. Red cross depicts SN. The dashed blue rectangle indicates
 1037 the 2015 study area shown in Figure 3. Gray arrows schematically depict the coastal branch of the
 1038 Pacific-derived Arctic water flow suggested by *Dmitrenko et al.* [2017].

1039



1040

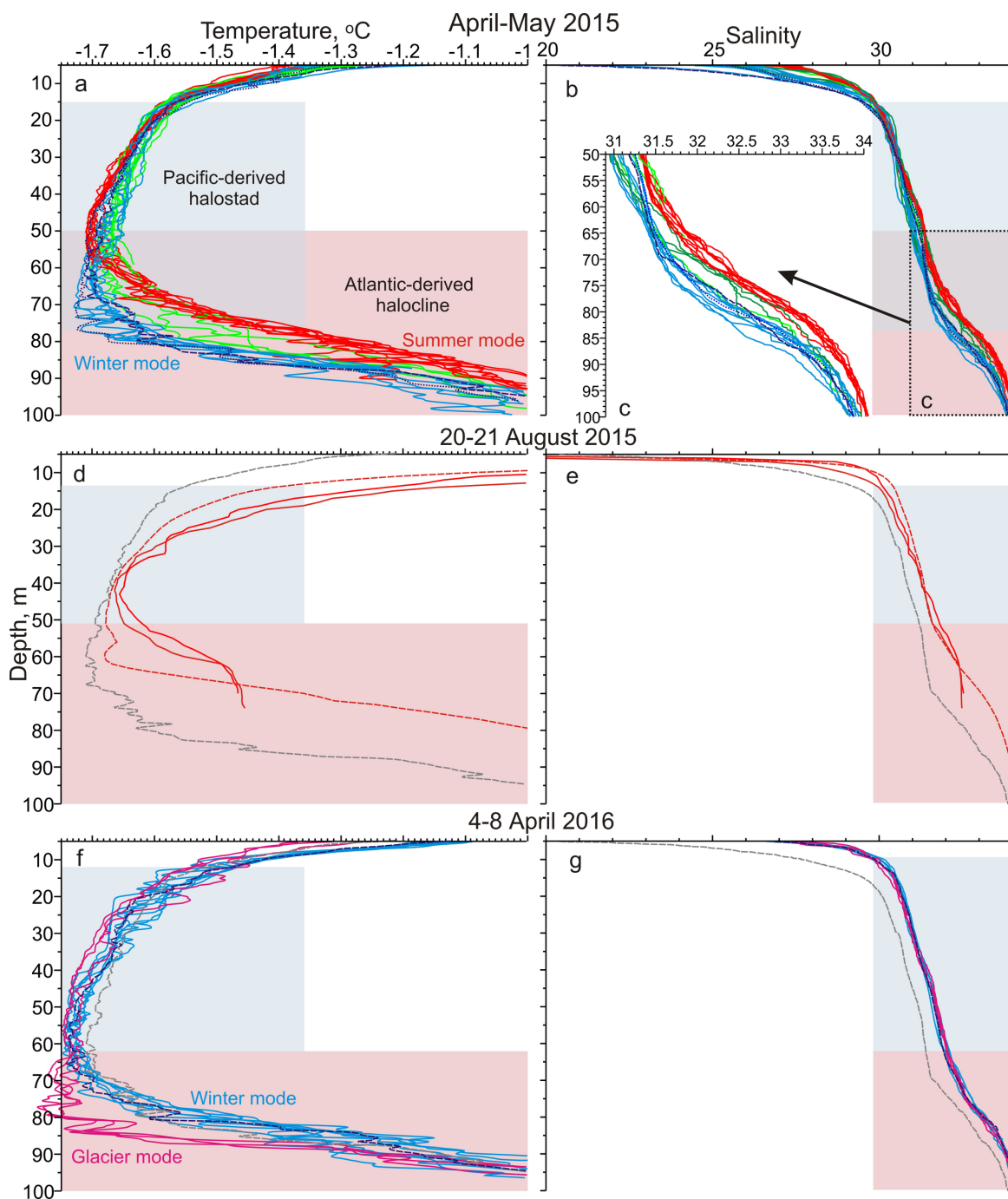
1041 **Figure 3:** (a) The Sentinel-1 C-band SAR image from 2 February 2015 with the CTD stations and
 1042 mooring overlaid. Colored circles identify CTD stations used for this research with CTDs showing
 1043 winter (blue), summer (red) and transitional (green) modes of the Pacific-derived halostad as
 1044 depicted with similar colors in Figure 5. Depth shown by white contour lines. Blue arrows indicate
 1045 the northern outlet glaciers of the Flade Isblink ice cap. The lighter areas indicate the multi-year
 1046 landfast ice (~2 m to > 4 m thick). (b) Aerial photo taken from the aircraft before landing at Station
 1047 Nord on May 2017 shows icebergs grounded on the marginal lateral moraine flanking the
 1048 southwestern rim of the glacier trough (credits: I. Dmitrenko).



1049

1050 **Figure 4:** The Sentinel-1 C-band SAR images from (a) 19 August 2015 and (b) 4 April 2016 with
 1051 the CTD stations and mooring overlaid. Colored circles identify CTD stations used for this
 1052 research with CTDs showing winter (blue), summer (red) and glacier (purple) modes of the
 1053 Pacific-derived halostad as depicted with similar colors in Figure 5. (a) The dark areas indicate the
 1054 open water. (c) Aerial photo taken over the tidewater glacier outlet in May 2017; purple arrow
 1055 highlights the glacier bay where CTDs occupied in April 2016 (credits: I. Dmitrenko). The spatial
 1056 scale at left bottom is approximate.

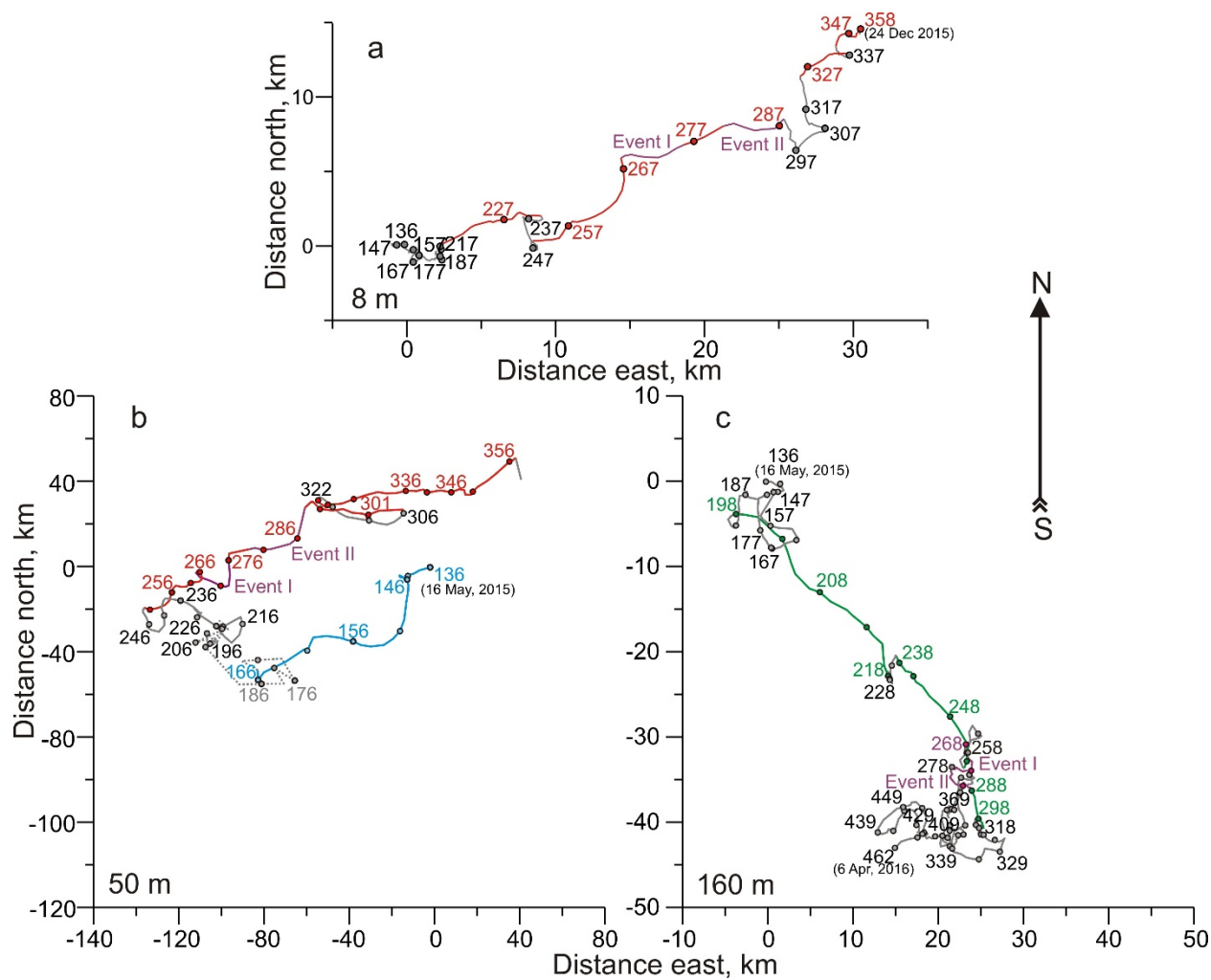
1057



1058

1059 **Figure 5:** Vertical distribution of (a, d and f) temperature ($^{\circ}\text{C}$) and (b, c, e and g) salinity over the
 1060 southeastern Wandel Sea shelf (>60 m depth) in (a,b,c) April-May 2015, (d,e) 20-21 August 2015
 1061 and (f,g) 4-8 April 2016 through the upper 100-m layer. Red, blue, green and purple lines indicate
 1062 the summer, winter, transitional and glacier modes, respectively. Dashed lines show moored ITP
 1063 profiles. Dotted lines in a and b are from station #65 (see Figure 3). Gray dashed lines in d-g are
 1064 the ITP profiles taken in 15 May 2015 as in a-c. Blue and pink shading highlights the Pacific-
 1065 derived halostad and Atlantic-derived halocline, respectively.

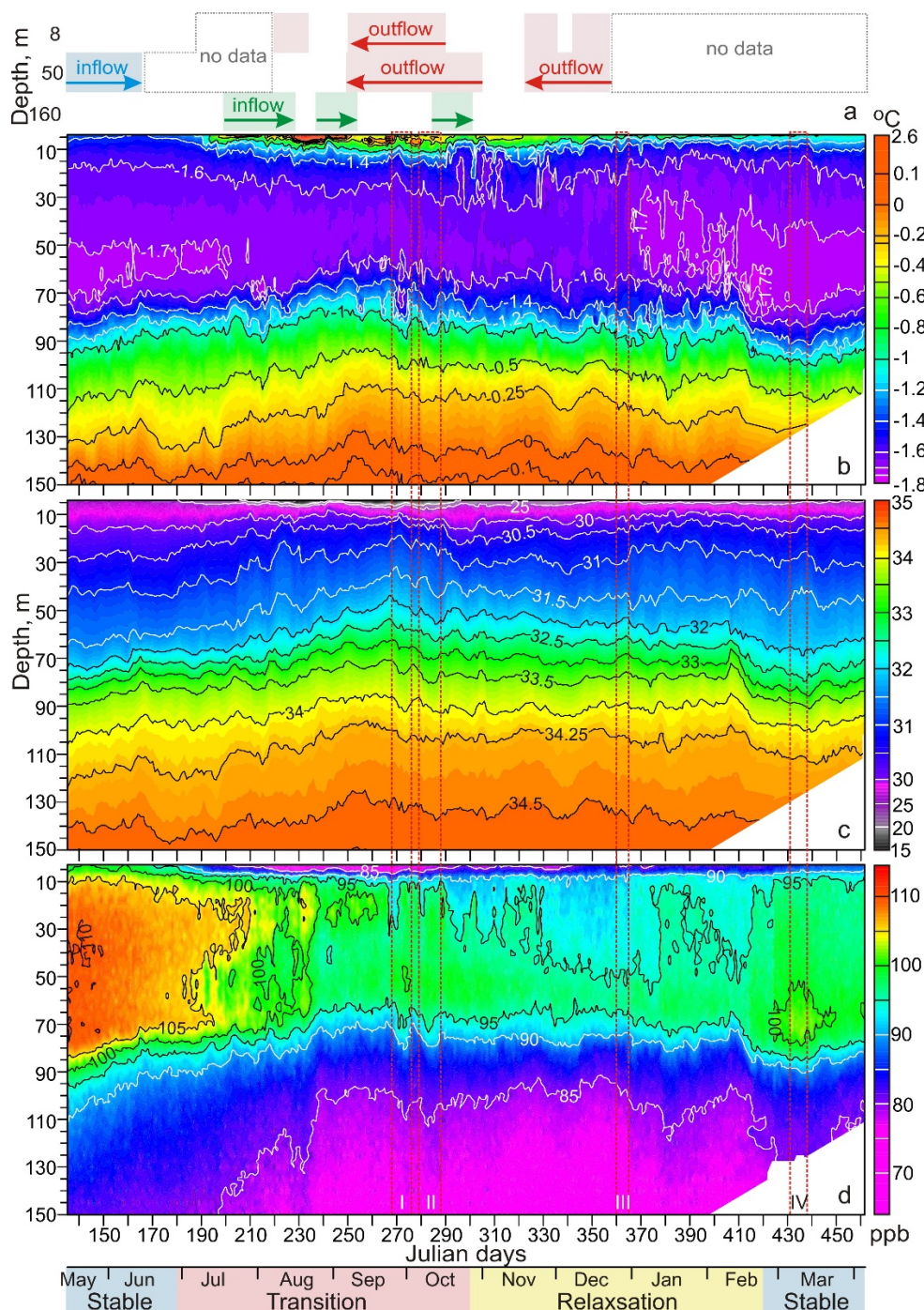
1066
1067
1068
1069



1070

1071 **Figure 6:** Progressive vector diagram for the ADCP 2-m binned current record at (a) 8 m, (b) 50
1072 m and (c) 160 m depth. Blue and green lines highlight on-shelf inflow (b) across the shelfbreak
1073 and (c) along the submarine glacier valley, respectively. (a, b) Red line highlights shelf outflow.
1074 Purple lines indicate storm events also depicted in Figures 7 and 9. Dashed line indicates no
1075 reliable data. Numbers show the Julian days.

1076



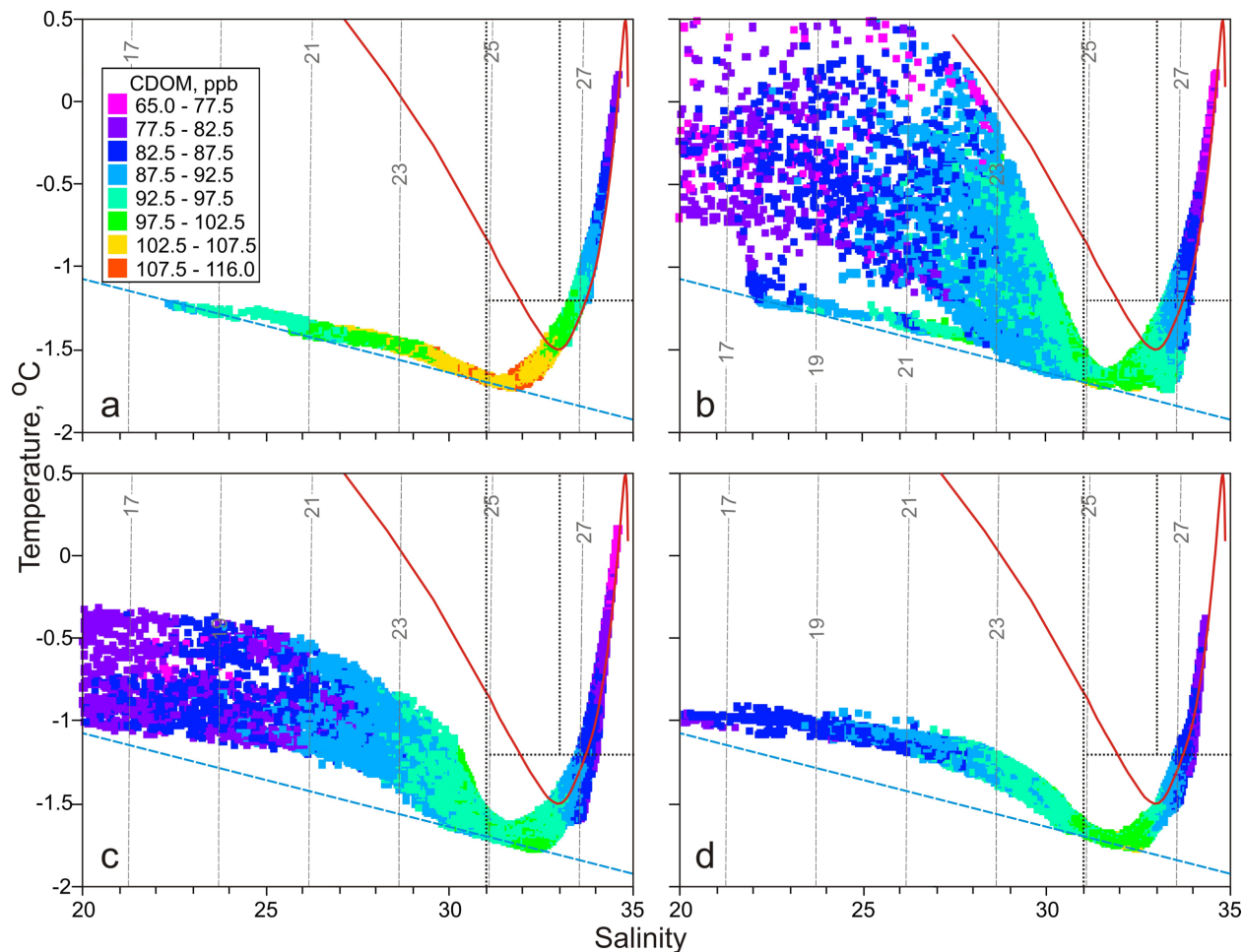
1077

1078 **Figure 7:** (a) Schematic depictions show the on-shelf inflow (blue and green shading and arrows)
 1079 and outflow (pink shading and red arrows) events based on ADCP data for (top) 8 m, (middle) 50
 1080 m and (bottom) 160 m depth. (b) Temperature ($^{\circ}\text{C}$), (c) salinity, and (d) CDOM fluorescence
 1081 (ex/em 370/460 nm, ppb) from the Ice Tethered Profiler (ITP) deployed over the southeastern
 1082 Wandel Sea shelf from 15 May 2015 to 6 April 2016. Red-dashed rectangular indicates storm
 1083 events associated with southerly and southwesterly winds over the Wandel Sea continental slope
 1084 with their reference numbers from I to IV at the bottom. Color shading at the bottom highlights
 1085 different periods of CTD and CDOM variability.

1086

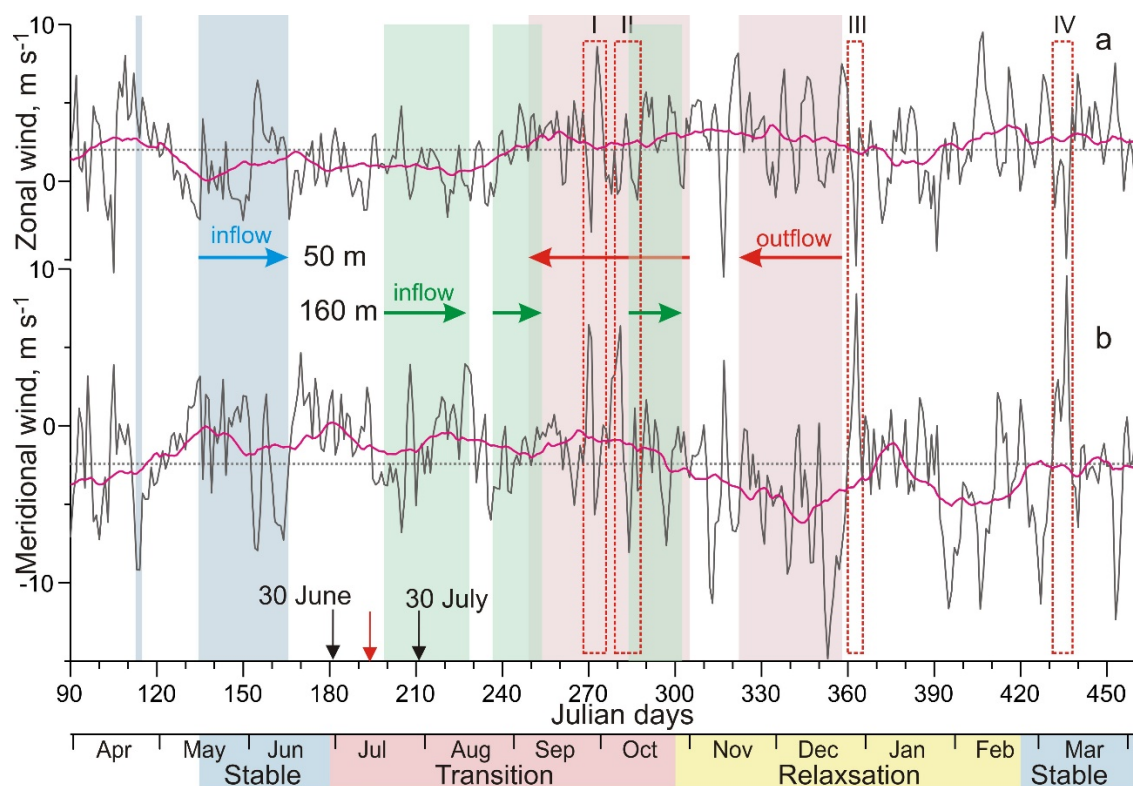
1087

1088



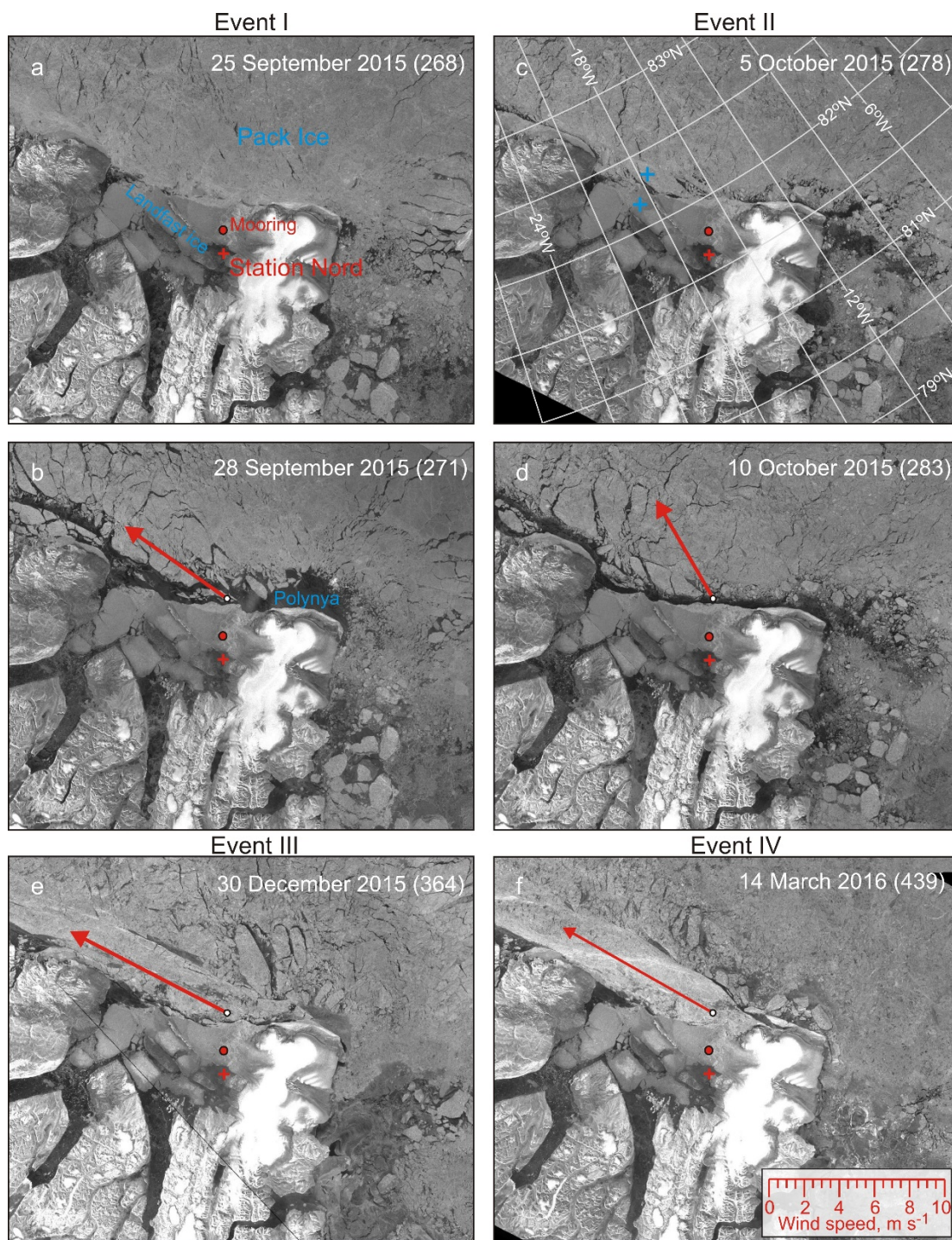
1089

1090 **Figure 8:** In situ *TS* scatterplots of the temperature, salinity and CDOM time series from the
 1091 mooring during (a) stable, (b) transitional, (c) relaxation, and (d) stable periods. CDOM
 1092 fluorescence (ppb) is shown in color. The gray dashed lines are potential isopycnals in kg m⁻³. The
 1093 dashed blue line is surface freezing temperature. Black-dotted lines indicate the bounds defining
 1094 the different water masses in the western Beaufort Sea following *von Appen and Pickart* [2012]:
 1095 the 33 line separates the Pacific ($31 < S < 33$) from the Atlantic ($S > 33$) water, and the -1°C line
 1096 separates the Pacific summer and winter water. Red line shows in situ mean *TS* diagram for the
 1097 cross-slope eastern Beaufort Sea section adopted from *Dmitrenko et al.* [2016].



1098

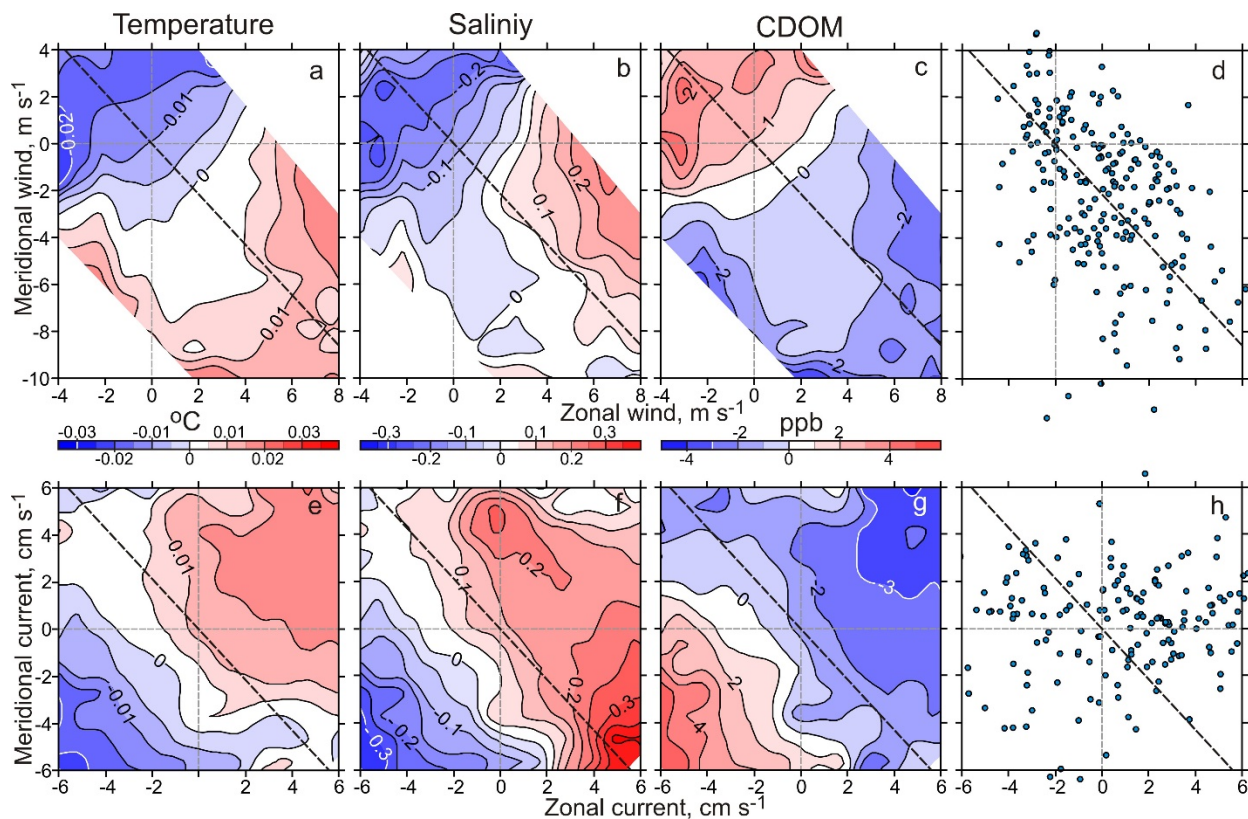
1099 **Figure 9:** Time series of the NCEP-derived 24-h mean 10-m (a) zonal and (b) meridional wind
 1100 (m s^{-1}) over the Wandel Sea continental slope at 82°N , 15°W (position depicted by white circles
 1101 in c-d) from April 2015 to April 2016. Purple line shows the 30-day running mean. Blue and green
 1102 shading and arrows highlight the on-shelf inflow at 50 m and 160 m depth, respectively. Pink
 1103 shading and red arrows highlight shelf outflow at 50 m depth. Red-dashed rectangular indicates
 1104 storm events associated with southerly and southwesterly winds over the Wandel Sea continental
 1105 slope with their reference numbers at the top. Color shading at the bottom highlights different
 1106 periods of CTD and CDOM variability as of Figure 7. Red arrow at the bottom identifies the day
 1107 when the landfast ice was collapsed over the Wandel Sea continental slope. The MODIS/TERRA
 1108 satellite images show the evolution of the landfast ice from (c) 30 June to (d) 30 July 2015. Red
 1109 circle and cross depict mooring and SN, respectively.



1110

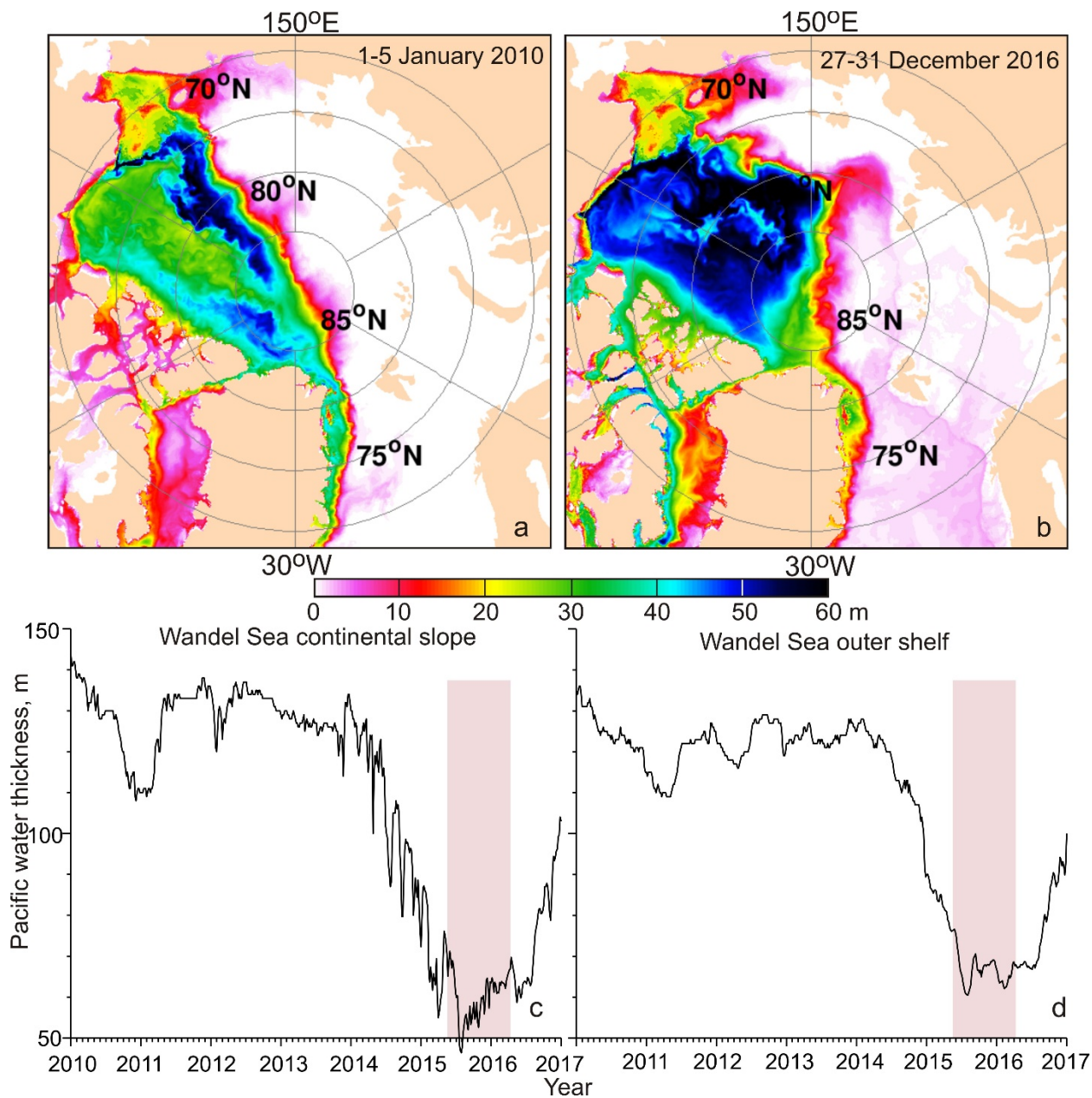
1111 **Figure 10:** The Sentinel-1 C-band SAR images taken over the Wandel Sea and NEW at the
 1112 beginning of storm events # (a) I and (c) II and 24-h following the meridional wind maxima over
 1113 the Wandel Sea continental slope for storm events # (b) I, (d) II, (e) III and (f) IV. Red arrows
 1114 indicate the 24-h mean direction and velocity of maximal wind according to scale shown in f. Red
 1115 circle and cross depict mooring and SN, respectively. (c) Blue crosses indicate positions over the
 1116 Wandel Sea outer shelf and continental slope where the time series of the PW tracers shown in
 1117 Figures 12c and 12d, respectively.

1118
 1119
 1120
 1121



1122
 1123
 1124
 1125
 1126
 1127
 1128
 1129
 1130
 1131
 1132

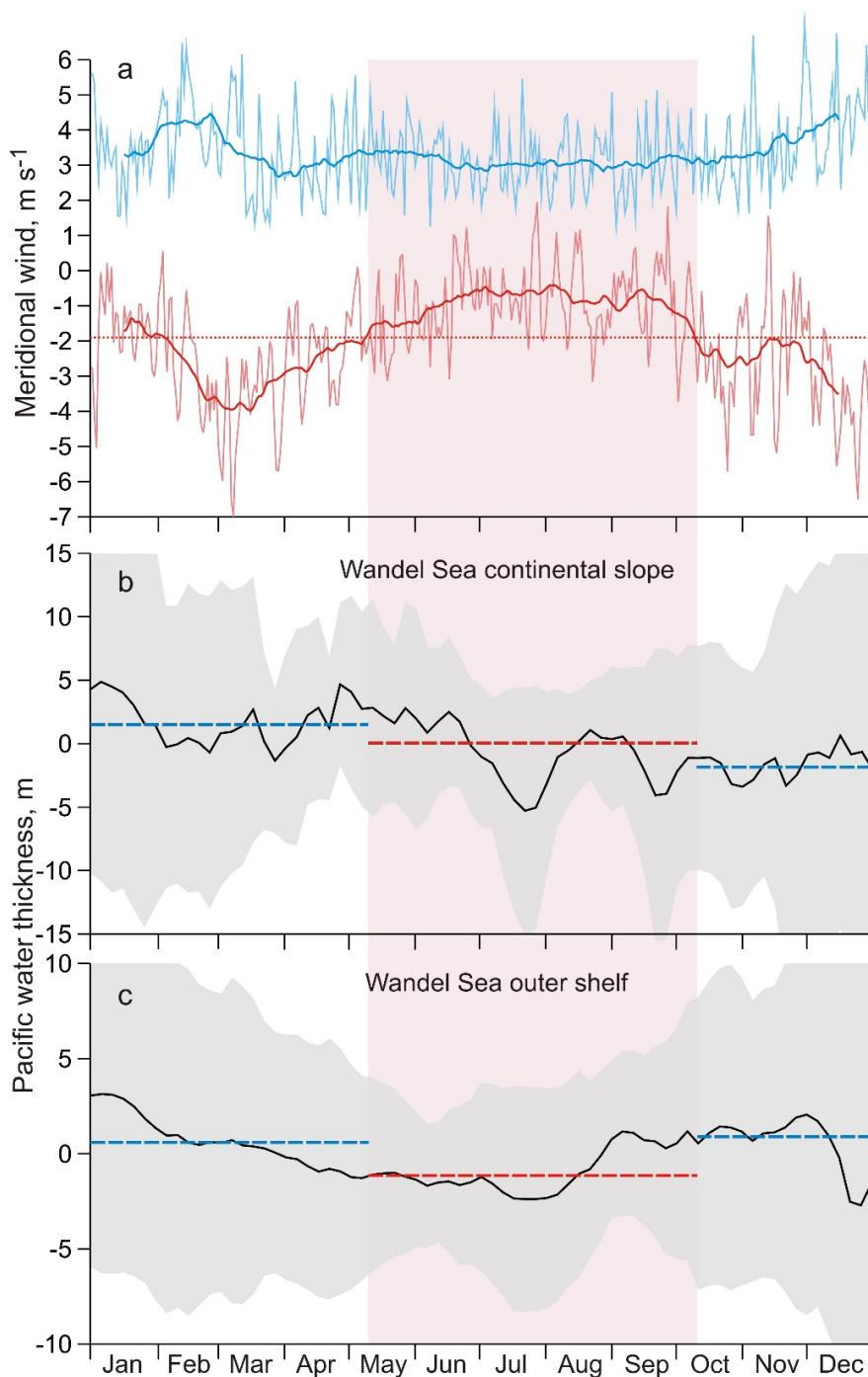
Figure 11: Color shading shows daily mean (a, e) temperature (°C), (b, f) salinity and (c, g) CDOM (ppb) anomalies at 50 m depth from the moored ITP versus NCEP daily mean 10-m wind over the Wandel Sea continental slope (top) and daily mean currents at 50 m depth (bottom) from 15 May to 26 December 2015. Scatter plots show daily mean (d) winds and (h) currents used for computing a-c and e-g, respectively. Black dashed line depicts the along-slope direction derived from the International Bathymetric Chart of the Arctic Ocean (IBCAO).



1133

1134 **Figure 12:** Simulated PW tracers concentration (m) for (a) 1-5 January 2010 and (b) 27-31
 1135 December 2016 and time series of the PW tracers integrated through the 20-85 m depth layer over
 1136 the Weddell Sea (c) continental slope at 82°20'N, 17°40'W and (d) outer shelf at 82°10'N, 18°40'W,
 1137 as depicted in Figure 8c. (c, d) Pink shading highlights period of mooring record.

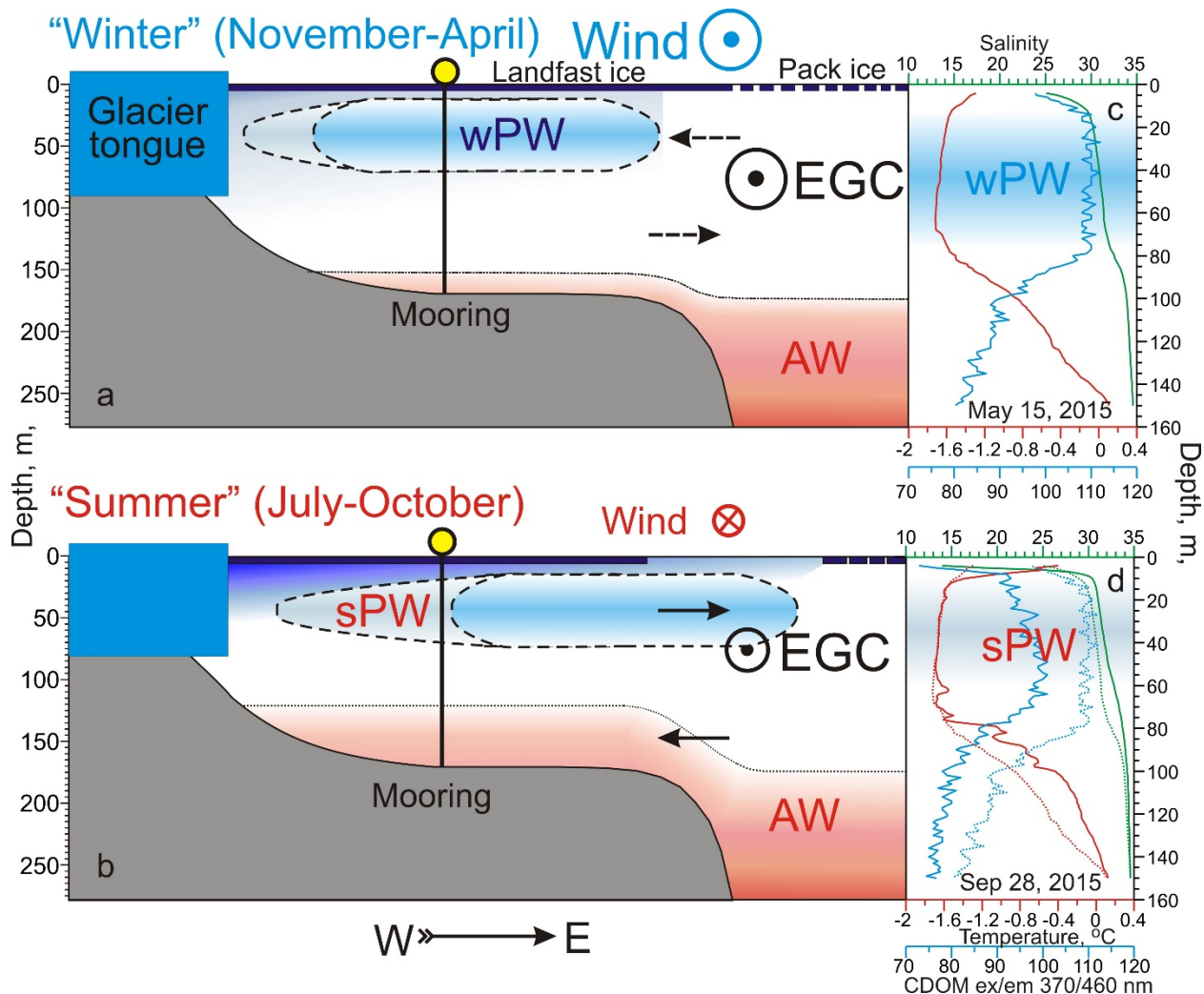
1138



1139

1140 **Figure 13:** (a) NCEP-derived 7-year mean (2010-2016) 10-m meridional wind (pink, $m s^{-1}$) over
 1141 the Wandel Sea continental slope with its standard deviation on the top (blue). Blue and red thick
 1142 lines show the 30-day running mean. The 7-year mean (2010-2016) anomalies of the simulated
 1143 PW tracers concentration anomalies (m) integrated through the 20-85 m depth layer over the
 1144 Wandel Sea (b) continental slope and (c) outer shelf. Gray shading highlights \pm one standard
 1145 deviation. Pink shading highlights period dominated by southerly winds. Red and blue dashed lines
 1146 show mean for periods dominated by southerly and northerly winds, respectively.

1147
1148
1149



1150

1151 **Figure 14:** Schematic depictions suggest lateral displacement of the Pacific-derived halostad in
 1152 response to (a) ‘winter’ (November-April) northerly and (b) ‘summer’ (July-October) southerly
 1153 wind forcing over the Wandel Sea continental slope with corresponding ITP CTD and CDOM
 1154 vertical profiles shown in (c) and (d), respectively. (d) Dotted lines show summer profiles for
 1155 comparison. Winter (cooler, fresher and CDOM enriched) and summer (warmer, saltier and less
 1156 CDOM) modes of Pacific-derived halostad are identified as (a, c) wPW and (b, d) sPW,
 1157 respectively.